

AN ABSTRACT OF THE THESIS OF

Michael Koopmans for the degree of Master of Science in Mechanical Engineering
presented on June 6, 2011.

Title: Exploring Experimental Test Stand Design and Operation within a
System Reliability Research Methodology

Abstract approved: _____

Irem Y. Tumer

In cases where complex systems routinely experience extreme operating conditions, preventative maintenance is often employed to guard against system failure. Yet, with accessible real-time data and the standard practice becoming prohibitively expensive, the test stand can serve as a vital contributor to the development of system health and reliability estimations. Utilizing a research methodology stemming from the prognostics and health management community, this thesis presents two separate, but related projects where test stands were tasked with populating component failure model databases. First, an actuator test stand design is assessed and optimized for in-flight experiments, where design recommendations are offered and the model is shown to rapidly develop electromechanical actuator test stand couplings. Second, a bearing test stand is used to derive empirical models for estimating the wear of polymer bearings installed on wave energy converters. Forming the foundation of the approach is an applicable wave model, sample data set, and method to impose loading conditions similar to that expected in real seas. The resulting wear rates were found to be linear and stable, enabling coarse health

estimations of the bearing surface. Further, limitations to the approach and plans for future experiments are also discussed. The work described in this thread provides a benchmark for a larger, more comprehensive reliability assessment of wave energy devices.

©Copyright by Michael Koopmans
June 6, 2011
All Rights Reserved

Exploring Experimental Test Stand Design and Operation within a
System Reliability Research Methodology

by

Michael Koopmans

A THESIS

submitted to

Oregon State University

in partial fulfillment of
the requirements for the
degree of

Master of Science

Presented June 6, 2011
Commencement June 2012

Master of Science thesis of Michael Koopmans presented on June 6, 2011.

APPROVED:

Major Professor, representing Mechanical Engineering

Head of the School of Mechanical, Industrial, and Manufacturing Engineering

Dean of the Graduate School

I understand that my thesis will become part of the permanent collection of Oregon State University libraries. My signature below authorizes release of my thesis to any reader upon request.

Michael Koopmans, Author

ACKNOWLEDGEMENTS

I wish to first thank my advisor, Dr. Irem Tumer for her encouragement and counsel throughout my last two years of research. It has been the most excellent learning experience.

I wish to express my appreciation for all the help and feedback Dr. Stone and Dr. Paasch have offered during my graduate studies. I would also like to thank Edward Balaban for his insight and guidance, in addition to my friends and fellow graduate students here in Corvallis for providing an outlet to decompress and discovering with me, all that Oregon has to offer. I also wish to acknowledge my friends from California for keeping me grounded and Cal Poly San Luis Obispo for the rigorous academic preparation.

And finally, I wish to thank my family for always being there for me. Thank you Mom, Dad, and Julie, for your unwavering support. I am eternally grateful to be your son and brother.

CONTRIBUTION OF AUTHORS

In the final manuscript presented, Mr. Stephen Meicke assisted with the bearing experiments, organization of the paper, and several rounds of text revisions. Dr. Robert Paasch provided the opportunity to conduct bearing wear experiments on the test stand of interest.

TABLE OF CONTENTS

	<u>Page</u>
1 General Introduction	1
1.1 Thesis Organization	2
1.2 Limitations of the Research	4
2 Reliability Based Design Recommendations for an Electromechanical Actuator Test Stand	5
2.1 Abstract	5
2.2 Introduction	7
2.3 Related Work	9
2.3.1 The EMA Test Stand	10
2.3.2 The Need for Availability	10
2.3.3 The Need for Reliability	11
2.4 Analysis Tool Characteristics	12
2.4.1 FMECA	12
2.4.2 Fault Tree Analysis	13
2.4.3 Reliability Block Diagram	13
2.4.4 Component representation	14
2.4.5 System Representation	15
2.5 Component Reliability Models	17
2.5.1 Reliability Data Sources	17
2.5.2 Base Plate	19
2.5.3 Actuators	20
2.5.4 Linear Rails and Guide Blocks	22
2.5.5 Sensor Features	23
2.5.6 Others	25
2.5.7 Summary	25
2.6 System Reliability Model Development	25
2.6.1 FLEA FMECA	26
2.6.2 FLEA Fault Tree Model	26
2.6.3 FLEA Reliability Block Diagram Model	29
2.7 Analysis Results	29
2.7.1 Fault Tree Analysis	30
2.7.2 Reliability Block Diagram Analysis	31
2.8 Design Recommendations	32
2.8.1 Ensure Alignment	33
2.8.2 Design for Quick Repair of Critical Components	33
2.8.3 Secure FLEA components	34
2.8.4 Increase Actuator Assembly Work Envelope	34

TABLE OF CONTENTS (Continued)

	Page
2.8.5 Avoid the Use of Steel Screws in Aluminum Plates	35
2.8.6 Ensure FLEA Enclosure is Free of Debris	35
2.8.7 Add Service Loops and Stress Relief to All Wiring	35
2.9 Conclusion	36
3 Electromechanical Actuator Test Stand Coupling Design to Support Actuator Prognostic Model Development	37
3.1 Abstract	37
3.2 Introduction	39
3.2.1 Paper Focus and Contributions	40
3.3 Background	42
3.3.1 Uncertainty in Design and Prognostics	43
3.3.2 Model Uncertainty	45
3.3.3 Load Uncertainty	46
3.3.4 Actuator Application	46
3.4 Overview of the Approach	47
3.5 Demonstration / Numerical Example	50
3.6 Discussion	63
3.7 Conclusion	65
4 Wave Energy Converter Bearing Health Estimation and Experimental Test Stand Benchmarking	67
4.1 Abstract	67
4.2 Introduction	69
4.2.1 Main Contributions of the Paper	70
4.2.2 Roadmap	71
4.3 Background	71
4.3.1 The Point Absorber	72
4.3.2 PHM Based Techniques	75
4.3.3 Test Stand Considerations	76
4.3.4 Modeling Considerations	76
4.4 The Wave Climate	77
4.4.1 Wave Data	78
4.4.2 The Sample Data Set	78
4.4.3 Choosing Experimental Cases	80
4.5 Experimental Design	80

TABLE OF CONTENTS (Continued)

	<u>Page</u>
4.5.1 Wave Modeling and Force Calculation	82
4.5.2 Experimental Case Parameters	85
4.5.3 Bearing Health Estimation	87
4.6 Experimental Setup	89
4.6.1 Bearing Material	89
4.6.2 Counterface	90
4.6.3 Test Stand	91
4.7 Results	92
4.8 Discussion	98
4.8.1 Effect of Counterface Roughness	98
4.8.2 Wave Modeling	99
4.8.3 Wear Data Quality and Health Estimations	99
4.8.4 Test Stand Effects	100
4.8.5 Lessons Learned	101
4.9 Conclusion	101
5 General Conclusion	103
5.1 Applications and Future Directions	103
Bibliography	104

LIST OF FIGURES

Figure	Page
1.1 A universal PHM research methodology.	2
2.1 The actuator assembly, where only one test actuator is connected to the coupling at a time.	11
2.2 Hole patterns on the base plate.	20
2.3 Tabs on the bottom of the actuator housing provide additional support and rigidity.	21
2.4 The thermocouple and accelerometer shown measure bearing raceway temperature and ball nut vibrations respectfully.	21
2.5 A graph depicting linear guide assembly failure rate (solid line) and THK rolling resistance, relative to a horizontal displacement.	24
2.6 System fault tree model. Top state is no/bad fault data, dropping into the central processor, data acquisition, sensors, actuators, and support hardware.	28
2.7 System reliability block diagram. START node on left initiates path from flight computer, into the system, ending with the base plate and other supporting structures.	29
3.1 An example comparison of two couplings with their load occurrence on the left and corresponding wear variable response on the right.	41
3.2 A top view of the actuator coupling currently installed on the FLEA [1].	43
3.3 A high level prognostic model [2].	45
3.4 Coupling layout showing design values used in the optimization.	52
3.5 Cross section view of the coupling shaft with applied and reaction force components.	54
3.6 The optimization model architecture.	59
3.7 Deflection plot for both materials.	60
3.8 6061-T6 Aluminum design variables.	61
3.9 1020 mild steel design variables.	62
3.10 Optimized actuator coupling solid model.	63
4.1 Oscillating wave energy converter devices.	72

LIST OF FIGURES (Continued)

Figure		Page
4.2	A generic linear power take-off point absorber WEC architecture layout, where relative motion between the buoy and spar provide energy conversion opportunities.	73
4.3	A universal PHM research methodology.	75
4.4	The total wave climate, where each bin contains the average number of hours for each sea state for an average year during the past six years (2005 - 2010).	79
4.5	Wave period distribution over the entire climate data set, with an average of 10.89 sec and a standard deviation of 2.95 sec.	80
4.6	Distributions of significant wave heights for the 10 -11 sec period bin with an average of 2.3 m and a standard deviation of 1.0 m. . .	81
4.7	A regular two dimensional wave with relevant parameters and coordinate system shown.	82
4.8	Example surface displacement and corresponding water particle velocities for a $H = 3$ m, $T = 12$ sec wave.	85
4.9	Example force oscillation imposed on the buoy by a passing $H = 3$ m, $T = 12$ sec wave, where F_d and F_i represent the individual components of F_x : the drag and inertial forces, respectively. The actual normal force applied to bearing sample was taken as the root mean squared value of the maximum F_x due to test stand limitations. . .	86
4.10	Counterface dimensions.	90
4.11	The bearing wear test stand.	92
4.12	Experiment case one, pressure = 334 kPa, maximum surface velocity = 0.66 m/s, mass = 3.382 kg.	93
4.13	Experiment case two, pressure = 500 kPa, maximum surface velocity = 0.1.25 m/s, mass = 5.000 kg.	94
4.14	Experiment case three, pressure = 202 kPa, maximum surface velocity = 0.55 m/s, mass = 2.045 kg.	94
4.15	Experiment case four, pressure = 445 kPa, maximum surface velocity = 0.69 m/s, mass = 4.442 kg.	95
4.16	Specific wear rates plotted vs. applied bearing pressure for all twelve test runs with the conservative model overlay (dotted line).	96

LIST OF FIGURES (Continued)

<u>Figure</u>		<u>Page</u>
4.17	An example wear estimation for the month of January 2011.	96

LIST OF TABLES

<u>Table</u>		<u>Page</u>
2.1	Components failure rates found within NPRD-95 and corresponding environmental factors within MIL-HDBK-217F.	18
2.2	Actuator failure and repair rates.	22
2.3	Sensor failure and repair rates.	25
2.4	A FMECA of the FLEA system, containing only custom components, where D = Detectability, O = Occurrence, and S = Severity.	27
2.5	ITEM toolkit fault tree analysis results.	30
2.6	ITEM toolkit reliability block diagram results.	31
3.1	Monotonicity Analysis.	58
3.2	Optimization results for 100 mm arm length.	61
4.1	Chosen test wave heights and periods.	81
4.2	Experiment Case Parameters	86
4.3	Determining each experimental case's sample size using the operational characteristic curves with $\alpha = 0.01$	88
4.4	Stable wear rates for each test run and their corresponding before and after surface roughness measurements (average, maximum, minimum).	97

Chapter 1 – General Introduction

Complex system design is an exhaustively iterative process that requires decades to perfect, particularly where extreme operating conditions exist [3, 4]. It is these operating conditions that render (from an engineer’s perspective) the success of a complex system be illustrated with reliability statistics and budget overruns. And so, typically during the design process, various test stands are built to prove concepts, validate mathematical models, and generally instill confidence in the system’s performance estimates. These estimates can range from an engine’s power output, to a communication antenna’s gain, to an actuator’s failure rate. The latter being used precisely as a means to quantify reliability. Here, the component failure rates and other related failure information are of great importance because they build a foundation for the system health management framework and ultimately, the system reliability estimations.

Therefore, a test stand can be tasked with validating, where applicable, the failure rate used within reliability calculations and system health decisions. In other words, by designing the test stand to impose comparable operating conditions, single or multiple components can be sacrificed to gain the necessary information for modeling the component’s failure (i.e., life), and subsequently the system’s health [5]. Yet, the quality and efficiency at which the test stand itself is designed and implemented can impact the system’s original cost projections, performance estimates, or project feasibility.

And so, a methodology born in the prognostics and health management (PHM) research community [6] was consulted to provide a platform on which test stand

research can be integrated into a larger, more comprehensive effort to assess system health. A general outline is shown in Fig. 1.1, where the path to implementing and relying upon a prognostic solution begins with high-level system requirements (health predictions for subsystems and / or the system itself) that define the subsequent metric, fault, and sensor selection process. Next, the third block deter-

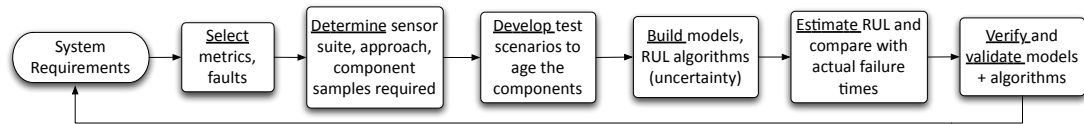


Figure 1.1: A universal PHM research methodology.

mines the most appropriate approach in terms of desired performance, available resources, and acceptable uncertainty to satisfy the component-level predictions. Here the proper number of samples to sacrifice for an accurate inference is also set. The fourth block ascertains the test scenarios, design of experiments, testing, and data collection, while the fifth block is dedicated to building models and remaining useful life algorithms for nominal and faulted conditions. The last two blocks encompass the health estimation and actual usage comparisons, in addition to the verification and validation sequences. A good application of the entire PHM research methodology estimated battery capacitance over time using high quality test chambers [7]. For this work however, only a few blocks of the methodology are addressed for two prognostic domains.

1.1 Thesis Organization

This thesis is presented in two parts: the first lies within the actuator prognostics domain, where questions contained in blocks three and four are addressed, while the second is concerned with polymer bearing prognostics and addresses questions

contained in blocks three, four, and five. In each part, a test stand was the fulcrum of research, where first, an actuator test stand design was optimized for electromechanical actuator experiments and second, a bearing test stand was employed to produce bearing health estimations. In summary, the purpose of this research is to provide the designer with insight for assessing test stand design aspects that affect failure information collection and ultimately, how to effectively use a test stand within a system's health estimation research methodology.

The two parts of this manuscript thesis are built off three papers that describe the effect of a prognostics and health management (PHM) based research methodology on test stand design and practice. Specifically, the application of electromechanical actuator failure experiments and wave energy converter bearing wear estimations. The first two papers make up part one, while the third manuscript is part two. The contributions of each paper are as follows:

- Treating the test stand as a system, reliability assessment procedures were applied to determine design issues that affect test stand availability and reliability to the researcher. Design modifications and recommendations are also suggested for future electromechanical actuator test stands.
- Using the original actuator test stand as an example, a coupling was optimized for a commercially available actuator to improve performance and failure data correlations. By implementing this model, researchers can rapidly develop their own electromechanical actuator test stand couplings.
- An initial effort to assess wave energy converter bearing health based on PHM techniques is described. Test stand benchmarking is conducted to classify polymer bearing wear for representative set of wave parameters.

1.2 Limitations of the Research

As with many research projects, there are use cases where the contributions are directly applicable and other, similar cases, where significant re-work would be needed. For the actuator test stand investigation, the contributions can be applied to the original actuator test stand that is currently in use [8] and future test stands with one load actuator and two test actuators, regardless the type of actuator. When considering the bearing test stand, the use case is limited to pressures and velocities safely achievable by the test stand. Therefore, applications of the bearing test stand can increase by enabling force (and consequently pressure) control coupled with a smoother, larger range of surface velocities.

Chapter 2 – Reliability Based Design Recommendations for an Electromechanical Actuator Test Stand

2.1 Abstract

The quality and robustness of data sets of faulted electromechanical actuators (EMAs) are necessary to strengthen aircraft prognostic data analysis of such systems. Primary flight surface control actuators are of particular interest because the lack of known failure data erodes the confidence of the component and subsequently sub-system health predictions. To aid in this research, an EMA test stand has been designed and built to help in predicting the life and wear characteristics of faulted actuators with respect to their nominal counterparts. Faults are injected into the actuator during in-flight experiments while actuator parameters are recorded and then post-processed on the ground. This paper provides a reliability and availability assessment of the current EMA test stand design. Using the performance history of similar components in the field, this work specifically demonstrates design aspects of the test stand that affect test system operation and fault data quality. The study has been conducted to validate the test stand design, as well as offer design recommendations to increase test stand availability to supply quality and robust fault to failure data sets.

Reliability Based Design Recommendations for an Electromechanical Actuator Test Stand

Michael T. Koopmans¹, Graduate Research Assistant, koopmans@engr.orst.edu

Rudolph C. Hooven¹, Graduate Student, hoovenr@onid.orst.edu

Irem Y. Tumer¹, Associate Professor, irem.tumer@oregonstate.edu

¹Affiliation : Oregon State University, Corvallis, Oregon 97330, USA

Annual Conference of the Prognostics and Health Management Society

PHM 2010

Oct. 2010, Portland, OR, USA

2.2 Introduction

Electromechanical actuators (EMAs) have been sought recently as the future of primary flight control surface actuation [9]. Centralized hydraulic and electrohydraulic actuators are the current state of the art and although their installations are well understood, they are inefficient, require massive amounts of maintenance, and are susceptible to single point-failures [10, 11]. Commercial airlines have used centralized hydraulics for over 30 years while the military has installed the electrohydrostatic actuators (EHA) onboard the most recent flagship aircraft: the F-35 joint strike fighter. EMAs provide an alternative to accomplish the same task while at the same time being operable in space, passively cooled, lighter, more maintainable, and easier to integrate both mechanically and electrically into the aircraft [12]. Therefore, they are of particular interest over a wide range of applications from ships [13, 14] to aircraft [15, 16, 17]. However, their benefits come with a price: the inherent failure modes within the EMA require an advanced prognostics and health management (PHM) system and/or condition-based maintenance (CBM) system to be installed, guaranteeing the actuation system is as reliable and robust as its predecessors. The task of the PHM/CBM system is to detect and isolate incipient and abrupt failure modes as well as predict their effect on primary actuator control performance [18]. As embedded diagnostic and prognostic technology matures, these systems can be implemented to complete life and mission critical tasks [19, 20]. The science of prognostics is often convoluted and difficult to apply to a complex system [21, 22, 23]. Yet, predicting faults in components whose environment is often highly stochastic can be made easier by employing knowledge bases of seeded failure data sets [24, 6]. Specifically, building test stands to inject known faults into components, running experiments in an en-

environment similar to their operating conditions, recording component parameters (motor current, temperature, position and velocity error rates, vibrations), and identifying fault signatures in the actual operating environments become very critical. This is due to the fact that prognostics cannot rely on mathematical models and real time data alone, because most diagnostic techniques assume the fault or failure is either physically and mathematically derivable, insensitive to extraneous variables, and uncorrelated with other features. In reality, one or more of these assumptions are not true [5]. The true fault signature is most often buried deep within the raw data and that very real fact is all the more reason to invest in the collection and study of quality failure data sets.

Very little failure data is publically available to the field of prognostics that is not from a laboratory setting or completely artificial [25]. To address this problem for actuators in particular, a body of research has emerged to not only seed failures in EMAs [26, 27, 28], but also to diagnose, predict, and control them when a failure does occur [29]. An EMA test stand is currently going through flight experiments at NASA Ames Research Center. To complement the design for fault seed experiments, a reliability and risk study must be completed, assessing the test stands effectiveness at providing a platform for those experiments [30]. Methods and techniques will be taken from a mature field of research that focuses on ascertaining system reliability [31, 32, 33, 34].

To address this need, this paper presents an availability and reliability study conducted on the original operational flyable EMA test stand design [35, 1] using three traditional fault and reliability analysis techniques, that is, FMECA, fault tree analysis and reliability block diagrams. The purpose of the test stand is to provide a platform for running seeded fault experiments onboard aircraft. This paper will help establish FLEA availability, as well as component and system reliability

characteristics of these actuators during operation and testing. The comparison of results from the different tools will help qualify the test procedures and the test stand itself for airworthiness and for verifying that the data obtained can be applied to actuator health predictions. The following sections present related background for the study, how the software tools calculate the desired metrics, uncertainties within the component models, followed by results, discussion, and design recommendations.

2.3 Related Work

One of the goals of prognostics is to supply information about component and system health in a timely manner to interested parties, including pilots (in case of flight-critical failures), maintenance crews (asset management), field captains (mission-critical failures), or even the aircraft itself (automatic reconfigurable control strategies). Having direct access to this information will improve air safety, cost of ownership, and time for repairs. The military has published handbooks NPRD-95 and MIL-HDBK-217F that contain high level component replacement information, but nothing regarding types of failures, fault signatures, or actuator class [36, 37]. The authors, in collaboration with NASA Ames, are beginning to build the knowledge base for EMA failures by means of an EMA test stand designed and built on behalf of NASA Ames Research Center. Having run flight test aboard a C-17 and scheduled for the UH-60 platform, the test stand has demonstrated it is operable in flight. At this stage, design improvements are sought, and can be made regarding the assumptions behind the fault injections, test procedures, and system operation; basically a study to decide the validity of inferences drawn from the data sets [1].

2.3.1 The EMA Test Stand

The EMA test stand, hereby referred to as FLEA (short for FLYable Electromechanical Actuator) is a proof of concept platform built in 2009 to record data of faulted EMAs passively operating onboard aircraft [35]. Installed as cargo, it contains three EMAs – one load and two test actuators coupled with electric magnets (Fig. 2.1), a computer and data acquisition system, several sensors, and an external shell filling a 450 mm cube. Adaptors for user/flight engineering interfaces are located on the outside of the shell. FLEA communicates with the flight data computer via serial or ethernet ports and obtains dynamic pressure, attack & incident angles, and other parameters to calculate an input load for the respective actuator. Each test actuator follows a flight profile in terms of position and velocity while a switch arbitrarily determines if the nominal or faulted actuator is in service. Each test actuator contains a sensor suite recording the same parameters: housing and ball nut vibration, motor and ball nut temperature, motor current, voltage, position, and velocity. These measurements are then recorded and available for download and post-processing once the flight has ended.

2.3.2 The Need for Availability

In the models used for this paper, the concept of availability is used and is hence defined briefly here. FLEA is unique in that it is not always operating, it undergoes preparations in the lab before each experiment onboard the aircraft. Therefore, any problem found during experiments can be addressed before the next one. Yet, during experiments, FLEA must operate as designed because if a failure was to occur, a great deal of time and money is wasted. A low probability of unavailability during any given flight time is desired.

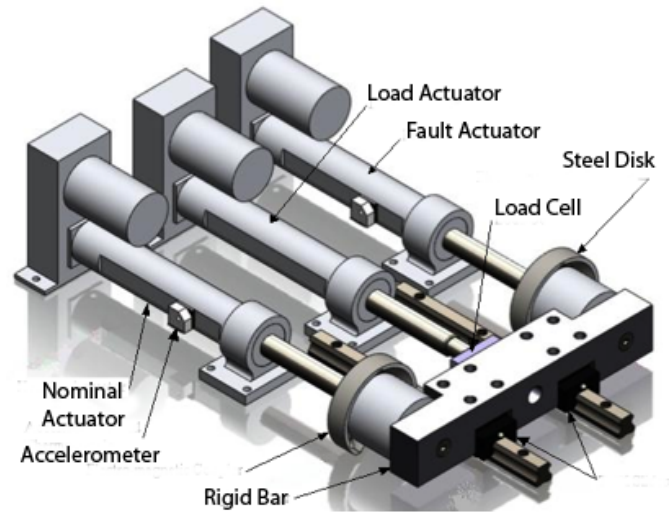


Figure 2.1: The actuator assembly, where only one test actuator is connected to the coupling at a time.

2.3.3 The Need for Reliability

In addition, the concept of reliability is used in the models that describe FLEA usage. For FLEA to be considered reliable, it will have to operate successfully for the duration of each flight, supplying quality data, without an unexpected or unscripted error. Since the period of time required to obtain the test results (beginning from fault inception to declared failure) is unknown, FLEA must be able to operate for an indefinitely long period of time; or in other words, have a high probability of reliability. FLEA is designed to operate in an aircraft environment with the assumption that no failures will occur in the testing apparatus that are not intentional. In a real world application, EMAs have proven to be unreliable with respect to their ball nut assemblies. Part of the purpose of this study is to determine what the useful life expectancies of FLEA components are as they were designed. A reliable test stand will operate free of unintended errors until the conclusion of the experiments. Risks associated with lowering this probability include failure to provide usable data, generating misleading data, or the life of

the load actuator (or even the actuator that is presumed nominal) being shorter than expected.

2.4 Analysis Tool Characteristics

Assessing system reliability can provide critical insights and information to the designer, including relative component contributions on a system level. By ensuring that each possible failure mode of each component is examined for its effect on the performance and reliability of the overall design, these methodologies greatly reduce omission errors and increase system functionality. The analysis of FLEA will be performed using ITEM Toolkit's modules for fault tree analysis (FTA), and reliability block diagrams (RBD) [38]. A separate FMECA will also be presented highlighting mechanical components custom built for the fault injection experiments.

2.4.1 FMECA

Failure Mode, Effects and Criticality Analysis (FMECA) is a widely used information tool in engineering [39, 40]. This reliability study will complete a brief FMECA of parts of the system not already covered in related work [27]. Expert knowledge will be the basis for the initial guesses of severity, detectability, and occurrence. These three parameters will be multiplied together to form the Risk Priority Number (RPN). By focusing design efforts on components with the largest RPNs while cross checking with the reliability model predictions, a more reliable FLEA may be designed. While FMECA is good at identifying initiating faults, and determining their local effects, it is not good at examining multiple failures

or their effects at a system level. The following tools allow for system inference of failure propagation.

2.4.2 Fault Tree Analysis

Fault Tree Analysis (FTA) is a top down approach to failure analysis [41]. The analysis begins with an undesirable top state and attempts to determine all of the component failures or combinations of failures that could contribute to that undesirable top state. As with FMECA, the data for this analysis relies on expert knowledge to correctly identify all of the contributing failures and the logical connections between them in addition to populating the model with reliability parameters.

The analysis tree is built with failure events coupled with logic gates to show the contributions of each component on system reliability. FTA can indicate how well a system can withstand single or multiple initiating faults and how those faults interact. For this study, each failure event is focused on mechanical failures with two reliability parameters failure rate and repair rate.

2.4.3 Reliability Block Diagram

A Reliability Block Diagram (RBD) is a graphical method for determining how component reliability contributes to the reliability of its overall system [42]. An RBD is a series of blocks representing system components that are connected in series or parallel depending on whether or not the system is operable given the failure. The system is available if and only if a linear unbroken path is possible from start to finish. For this study, each component is given a failure and repair

rate, assuming that after each failure the system is unavailable for the duration of the failed components repair rate. Both FTA and RBD return the same probabilities: system unavailability and reliability, along with percent of component contributions to system reliability.

2.4.4 Component representation

The homogeneous Poisson process is an appropriate preliminary model to employ for representing component failure rates in reliability block diagrams and fault tree analyses [43]. Consider a component with attributes λ_i and μ_i denoting mean failure rate relative to the total time (including repair durations) and mean component repair rate for each failure, respectively. The value λ_i can be calculated by dividing the number of component failures over a period of time by the period length (include repair times). The value μ_i can be calculated by dividing the number of component failures by the sum of repair times over a period of time. For example, if a component took 48 hours to repair once, its repair rate value would be 0.0208. Hence, the component model describes the random failures and repairs of the component in rate per unit time, is completely described by the two parameters λ_i and μ_i , and consequently holds the following assumptions:

1. Component failure rates do not change with time
2. Components experience random failures in time, independently of each other, and each failure entails a random duration of repair before the component is put back into service
3. Failed component repair duration is independent of the states of other components

4. The component faults within the system are ergodic, that is, the model employs a statistical concept stating that inferences are possible about a system over a short period of time that hold regardless of how long it has been in operation.

The reliability models will use the following equations to calculate both component and system probabilities and percentages. The following equation determines the probability that a component ($i = 1$) is unavailable for operation at any given time t (Eq. 2.5), known as component unavailability [38].

$$Q(t) = \frac{\lambda}{\lambda + \mu}(1 - e^{-(\lambda + \mu)t}) \quad (2.1)$$

The probability that a component will fail per unit time t , given that it was working correctly at time zero, is denoted as the component failure frequency (Eq. 2.2).

$$\omega(t) = (1 - Q(t))\lambda \quad (2.2)$$

2.4.5 System Representation

Once each component is modeled using dedicated failure and repair rates, cut sets must be defined. A cut set is the minimum set of components whose joint failure results in system failure. The failure frequency of an individual cut set is shown in Eq. 2.3:

$$\omega_{\text{CutSet}} = \sum_{j=1}^n \omega_j \prod_{i=1, i \neq j}^n Q_i \quad (2.3)$$

where n is the number of events within the cut set, ω_j is the failure frequency of the j^{th} event in the cut set, and Q_i is the unavailability of the i^{th} event in the cut set. The failure frequency of the system is shown in Eq. 2.4:

$$\omega_{\text{System}} = \sum_{i=1}^n \omega_{\text{CutSet}(i)} \prod_{j=1, j \neq i}^n (1 - Q_{\text{CutSet}(j)}) \quad (2.4)$$

where n is the number of cut sets within the system, $\omega_{\text{CutSet}(i)}$ is the failure frequency of the i^{th} cut set, and $Q_{\text{CutSet}(j)}$ is the unavailability of the j^{th} cut set. Next, the overall system reliability is calculated using the system unavailability, given by Eq. 2.5:

$$R(t) = e^{-(1-Q(t))} \quad (2.5)$$

Reliability is defined here as the probability the system is operating from time zero to time t , given the system was repaired to an operational state at time zero. Another parameter of interest is the conditional failure intensity (CFI) seen in Eq. 2.6, which represents the probability the system will fail, given it was working as designed at time 0.

$$\lambda(t) = \frac{\omega_{\text{System}}(t)}{1 - Q(t)} \quad (2.6)$$

Finally, to determine a specific events contribution to the system unavailability, the Fussell-Vesely importance measure is used, shown in Eq. 2.7.

$$IMP_{FV} = \frac{\sum Q_{CSwithBlockEvent}}{\sum Q_{CSTotal}} \quad (2.7)$$

Here, the metric sums the cut set unavailability given a specific failure with respect to total cut set unavailability. A change in the unavailability of a high importance valued event will have a significant effect on system unavailability.

To summarize, component unavailability and failure frequency will be computed for the system calculations, failure frequency is the probability of a failure within time t , independent of whether a failure has occurred before time t . The reliability and the conditional failure intensity metrics give pure values for the probability of a working system and no failures occurring during operational time. Keeping all this in mind, we can proceed with the mathematical modeling framework. However, several uncertainties must be considered regarding component integration and design before failure and repair rates are populated, discussed next.

2.5 Component Reliability Models

The following discussion is intended to analyze potential sources of model uncertainty and the effects on the components failure and repair rates.

2.5.1 Reliability Data Sources

In order for the analysis tools to be used, each component must be linked with a failure rate (usually in failures per 10⁶ hours) and repair rate (number of repairs per duration of repair). NPRD-95 and MIL-HDBK-217F reliability data is derived from maintenance records collected from 1970 to 1994 and statistically analyzed to a standard measured in failures per million cycles; they will be the primary source of failure information for this study. The fact that this information was collected from actual field data increases the confidence of the model results. While the failure data is not specific to any particular part or manufacturer, it is a good indication of what can be expected from any given class of part. Neither handbook

contains repair rates, therefore, they will be estimated for all components based on expert knowledge of FLEA during building and testing [35]. Also, to complete the models, failure rates of components not contained within the handbooks were estimated by the authors.

For this study, it is assumed that the airborne rotary wing (ARW) or helicopter environment can be used to adjust published reliability data numbers. Failure rates under this designation generally have higher failure rates than those installed on ground units or other airborne platforms. Tbl. 2.1 shows critical FLEA component failure parameters. In this table, GB indicates a ground laboratory assignment, AI

Table 2.1: Components failure rates found within NPRD-95 and corresponding environmental factors within MIL-HDBK-217F.

Component	Environment	Failures per 10^6 hrs	Factor
Linear EMA	ARW	1108	16
Linear EMA	GB	78	1
Accelerometer	AI	603	6
Thermocouple	ARW	63	16
Optical Encoder	GM	206	7
Load Cell	GF	22	2

indicates general airborne inhabited areas without environmental extremes, GM indicates equipment installed on wheeled or tracked vehicles, and GF indicates ground fixed position. The purpose of Tbl. 2.1 is to show the relative failure values of similar components assumed to be designed and installed properly. For this reason, if the data found for FLEA components was not directly taken from the ARW environment, the actual failure rates were multiplied by the appropriate factor. However, the two components taken directly from ARW have been multiplied by an additional factor based on built in design modifications for measuring ball

nut vibrations. Furthermore, knowing FLEA was constructed as a prototype, it is safe to assume that the component failure and repair rates will be much larger.

Repair rates will be estimated in terms of business days for completion including time for: removal, shipping, custom machining, installation, calibration, and testing. For example, the linear guide assembly repair rate is 0.0416 or one repair per 24 business hours.

2.5.2 Base Plate

The foundation of the test stand is the base plate it constrains all actuator and linear rail degrees of freedom. Vertical displacement and two rotational degrees of freedom are constrained with the top face of the plate while the remaining two displacements and one rotational degree of freedom are constrained by the hole patterns. FLEA reliability is affected through misalignment of the actuator and linear guide assemblies and indirectly from the strength of aluminum threads within the base plate. Errors in the hole patterns for the actuator mounts and linear rails as seen in Fig. 2.2 easily propagate to interacting components and the fault data produced. Steel fasteners gall aluminum threads quickly as the linear rails have been seen shifting during lab experiments and considering the high vibration environment of a helicopter, the threads become a much more significant design challenge. As for assigning a failure rate, the rate due to fully reversed shear loading has been calculated as negligible, but thread failure rate due to fastener insertion and removal has been estimated as $2.5 * 10^{-4}$ per thread: assuming the thread strips after 100 secure cycles and an average of 1 secure cycle per 40 hours. Furthermore, base plate repair rate has been estimated at 0.0125.

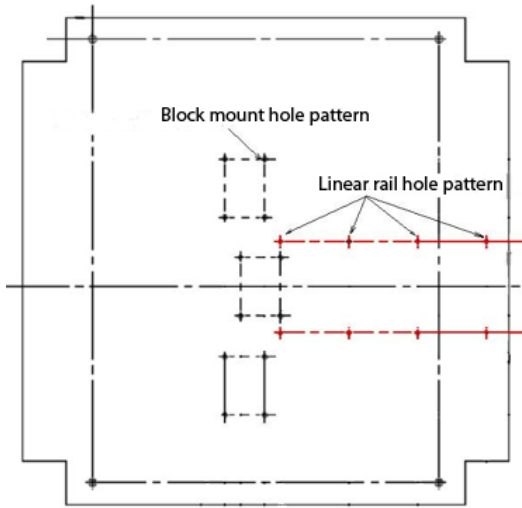


Figure 2.2: Hole patterns on the base plate.

2.5.3 Actuators

Three variables negatively affect the reliability of the three actuators installed, including their alignment relative to each other and to the linear guide assembly, coupling to the guide assembly, and fault modifications. Throughout the design process it was assumed that the actuators would travel parallel to each other and the linear rails. Misalignment however, has proven to be a very real problem in both actuator performance and data collection. During misalignment, the motor will draw additional current to overcome the additional resistance required to travel the same distance shortening useful actuator life and masking the true motor current signal with a false one. Next, space constraints required tabs to be welded under the gearbox casing for added support and attachment to the base plate (Fig. 2.3). These actions are not manufacturer approved and introduce misalignment issues. Next, the test actuators couple to the rigid bar via electric magnets and steel disks threaded over the actuator stud. These disks (seen on the right of Fig. 2.4) have unthreaded themselves during testing, ultimately resulting in zero actuator

coupling. Assuming the actuator stud threads are rolled steel and experience 100 lbf of fully reversed tensile loading, fatigue analysis estimates 7.45×10^9 cycles until thread failure. Of course the threads do not undergo pure tensile loading due to alignment issues, but for testing purposes thread failure is negligible. But, the loosening of the steel disk is not, while it may shear threads if aggravated. Also, several modifications to the actuator housing were completed so that sensors could monitor important measurements, particularly aspects of the ball nut (Fig. 2.4).

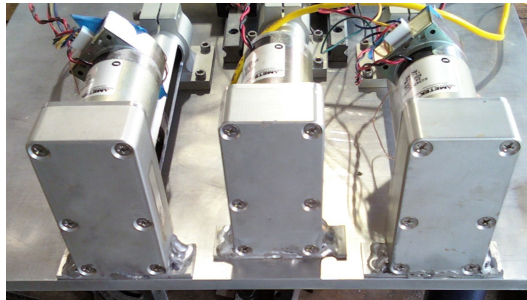


Figure 2.3: Tabs on the bottom of the actuator housing provide additional support and rigidity.

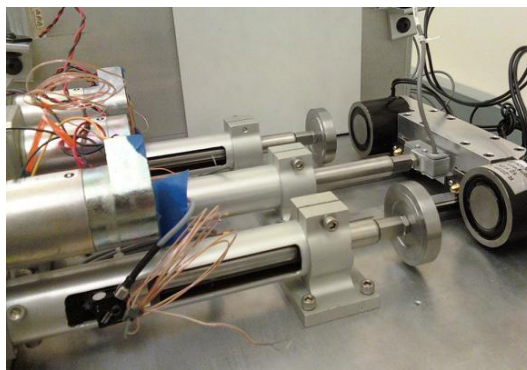


Figure 2.4: The thermocouple and accelerometer shown measure bearing raceway temperature and ball nut vibrations respectively.

Here, the seals have been bypassed and the lead screw is completely exposed to the environment, exacerbating bearing and ball nut debris problems. In general, flight certified actuators contain a thrust bearing for alleviating radial loads on the ball

bearings, but one does not exist for the actuators FLEA is testing. Nevertheless, each actuator is assigned a different failure and repair rate as seen in Tbl. 2.2. The

Table 2.2: Actuator failure and repair rates.

Actuator	Failure Rate	Repair Rate
Load	$2.86 * 10^3$	$1.38 * 10^{-2}$
Nominal Test	$3.32 * 10^{-3}$	$1.04 * 10^{-2}$
Faulted Test	$5.52 * 10^{-3}$	$0.83 * 10^{-2}$

logic behind the failure rates is based first off the original 1108 failures per 10^6 hours value in Tbl. 2.1, factors for the quality of the actuator, fault modifications, alignment (tolerance stack up from the base plate, actuator block mounts, rigid bar, and linear rails contribute to a vertical misalignment of up to 0.01 inches), couplings, and the load actuator for operating twice as long as either test actuator. For estimation purposes, these values are reasonable for a prototype test platform.

2.5.4 Linear Rails and Guide Blocks

The linear rail and guide block assembly is the foundation of the coupling, leading the actuators along a linear path and supporting the electric magnet. Positioning the rails relative to the actuators is a significant step for assuring quality FLEA operation. The linear rail manufacturer publishes formulas that will help predict the life span of their slides based on an applied radial load P , as shown in Eq. 2.8,

$$50\left(\frac{C}{P}\right)^3 = \text{Life(km)} \quad (2.8)$$

where C is the basic dynamic loading for the model of slide (8.33 kN). Misalignment causes the applied load and although this load is difficult to calculate, the manufacturer publishes empirical data linking vertical and horizontal displacement with a rolling resistance [44] as well. Vertical misalignment is not an issue with the linear rail life estimate as the guide block is able to absorb a vertical displacement between the two rails up to 0.01 inches and the current tolerance is below that value. Horizontal misalignment however is a significant issue as base plate machining may easily produce tolerance errors where upon a displacement of 0.004 inches imposes almost 6 extra lbf of rolling resistance. Fig. 2.5 is used to infer the linear guide assembly failure rate. The applied load P is derived by straining the rigid bar for a displacement value, while the 4 inch travel along the rail is completed an average of once per ten seconds. Since the experimental failure rates for the linear guide assembly were determined based on data from slide performance in a laboratory setting, the actual failure rate was multiplied by a factor of ten to approximate a helicopter environment. Therefore, assuming a 0.003 inches horizontal misalignment, the failure and repair rate for the linear rail and guide block assembly were set at $2 * 10^{-30}$ and $4.16 * 10^{-2}$ respectively.

2.5.5 Sensor Features

Equally as important as the components they are attached to, the sensors must operate and record data reliably. Their installations are of particular importance because of the prototype nature of FLEA. Four accelerometers, four thermocouples, and one load cell are the most critical sensors because they measure essential parameters for the fault data sets, are exposed to the environment, and require wires plus signal conditioning. The ball nut sensor installations require machining of the

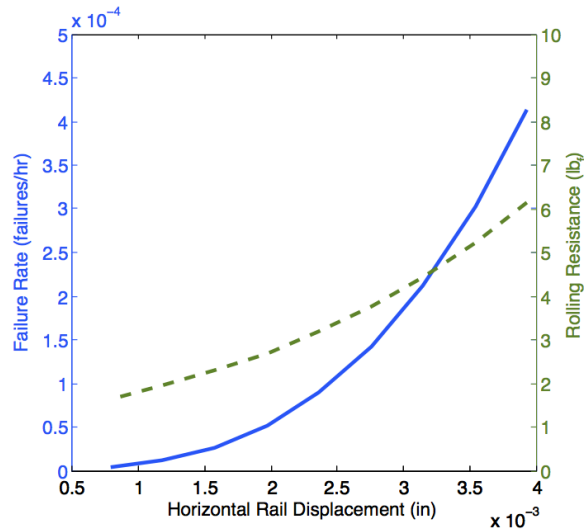


Figure 2.5: A graph depicting linear guide assembly failure rate (solid line) and THK rolling resistance, relative to a horizontal displacement.

actuator housing for access and careful attachment and routing of accelerometer and thermocouple wires. The thermocouple is located along the bearing raceway inside the ball screw assembly, while the wiring to the signal conditioning board is delicate. The accelerometer mounts to a metal block glued to the ball nut while a few 4-40 threads secure the sensor in place. The load cell is rigidly connected to the load actuator and rigid bar using two threaded bolts. Tbl. 2.3 shows the suggested failure and repair rates within the models.

Originally taken from Tbl. 2.1, the sensors were multiplied by the environmental factor and corresponding design uncertainties and divided by 106 to arrive at their current value. The accelerometer bolt has loosened during testing and come in contact with the actuator housing, rendering the experiment useless and along with the load cell, is subject to high transient vibrations during testing and experiments. The failure rates reflect the designers concern about flight environment effect on critical sensors.

Table 2.3: Sensor failure and repair rates.

Component	Failure Rate	Repair Rate
Accelerometer	$7.60 * 10^{-3}$	$4.16 * 10^{-2}$
Thermocouple	$1.26 * 10^{-3}$	$2.50 * 10^{-2}$
Load Cell	$6.16 * 10^{-4}$	$4.16 * 10^{-2}$

2.5.6 Others

Components not included in the handbooks, too abstract to calculate, or not considered critical to FLEA reliability are given an average failure rate of $2.0 * 10^{-4}$ and $1.3 * 10^{-2}$ repair rate. These components are either over-designed, electronic, or software related.

2.5.7 Summary

This section has presented critical FLEA components and their integration issues with the rest of the system and how they affect overall reliability. The following models will indicate the component contribution to system reliability, opening the design for needed changes.

2.6 System Reliability Model Development

With the necessary components thoroughly analyzed with respect to their reliable generation of quality data sets, ITEM Toolkit can be used next to calculate the system parameters of interest: unavailability, reliability, failure frequency, and individual component contributions to system availability. A FMECA is presented along with fault tree and reliability block diagrams developed using ITEMs modules.

2.6.1 FLEA FMECA

The FMECA presented in Tbl. 2.4 is the standard benchmark for critical component identification. Completed from the original FLEA designer and testers point of view, it encompasses custom FLEA components and actuator modifications not covered in previous detailed FMECAs [27]. The table focuses on FLEA installation and operation. An interesting note is to see how the risk priority numbers and Fussell-Vesely values correlate.

2.6.2 FLEA Fault Tree Model

The FLEA fault tree model is shown in Fig. 2.6. The fault tree has a top state of bad/no data, meaning the analysis focused on finding origins of the measurement and recording (or lack thereof) of non-quality data; non-quality data being an unreliable source in actuator health predictions. The model begins with identifying the last place the data resides before download after flight experiments on the computer hard disk. From there the model propagates through the electrical components followed by the mechanical components, stopping at the FLEA structure. Most of the electrical and computing entities of FLEA were not populated with failure or repair rates because they were considered insignificant relative to their mechanical counterparts and little justifiable reliability information is available. Each of the initiating events (round symbols) represents a component of the test stand that may introduce or cause misleading data. Primary focus is on the bottom two levels of the tree; here the sensors, couplings, and actuators reside inside the actuator assemblies.

Table 2.4: A FMECA of the FLEA system, containing only custom components, where D = Detectability, O = Occurrence, and S = Severity.

System	Component	Fault	Failure	D	O	S	RPN
Actuators	Load Actuator	ex. duty cycle	no force control	3	6	8	144
		misalignment	bad data	6	5	3	90
	Nominal	misalignment	bad data	6	5	3	90
	Faulted	fault inj. mod	no data	5	5	8	200
Coupling	linear rail	misalignment	overloading	4	8	5	160
		build error	bad data	5	3	5	75
	guide block	misalignment	bad data	4	8	5	160
		overloading	flaking / bad data	6	4	3	72
	load cell	overloading	no force control	5	5	9	225
		short circuit	no force control	5	1	8	40
		open circuit	no force control	5	1	8	40
	rigid bar	misalignment	bad data	3	4	5	60
	electric magnet	open circuit	no couple/no data	7	1	8	56
		short circuit	no couple or data	7	2	8	112
steel disk	loose thread	liberation	6	7	9	378	
fasteners	strip thread	bad data	3	6	8	144	
Structures	base plate	thread strip	bad data	8	7	8	448
		hole accuracy	bad data	3	4	4	48
	tslot	loose fastener	inc. vibrations	8	2	4	64
Data Acquisition	ball nut mount	casing contact	no vibration data	4	3	9	108
		high vibration	no vibration data	3	3	7	63
	coupling	no vibration data	7	4	7	196	
	thermocouple	ground	no temp. data	3	4	7	84
		severed wired	no temp. data	7	3	7	147
	signal processing	open circuit	no data	3	2	5	30
		short circuit	no data	3	3	6	54

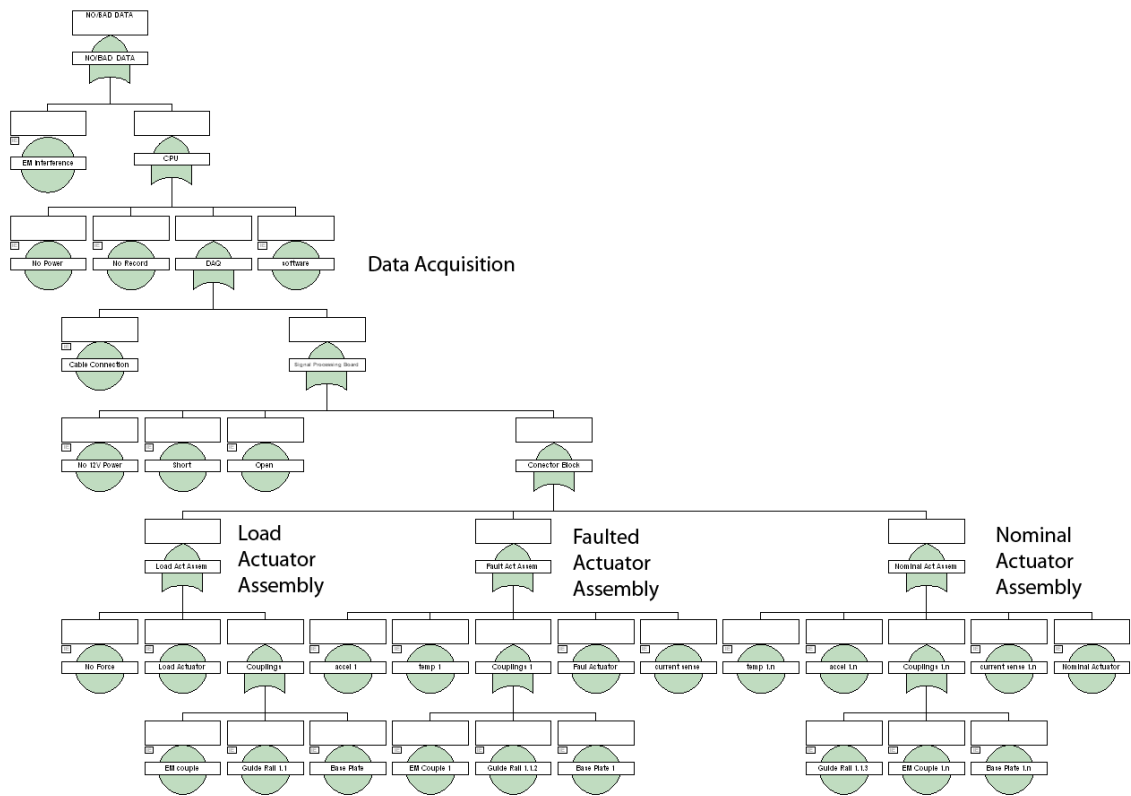


Figure 2.6: System fault tree model. Top state is no/bad fault data, dropping into the central processor, data acquisition, sensors, actuators, and support hardware.

2.6.3 FLEA Reliability Block Diagram Model

The FLEA reliability block diagram is shown in Fig. 2.7. Starting with the load actuator, mechanical energy is imposed on the actuator assembly for the duration of the flight experiment. A linear force is transferred to the coupling while an equal and opposite force is transferred to the actuator mount. The nominal and faulted test actuators distribute energy to their respective sensors, followed by the securing components to the base plate. For availability verification, a node exists after each parallel group of components that requires all paths flowing into it, be available for successful system operation.

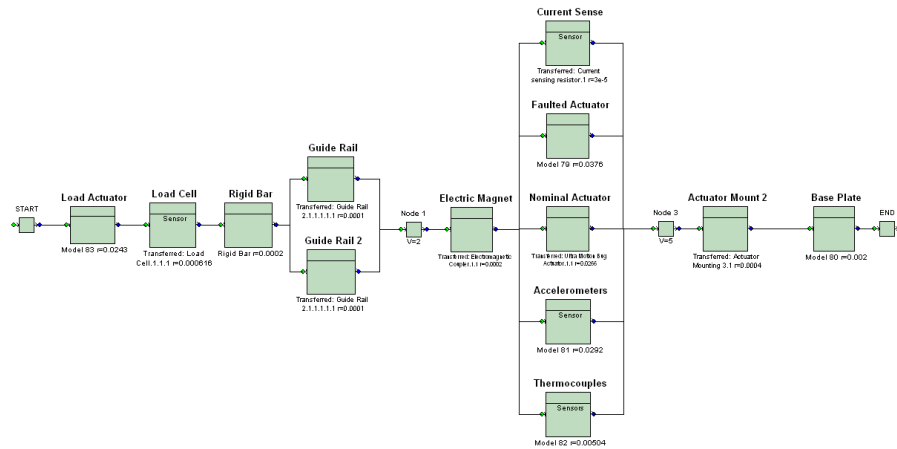


Figure 2.7: System reliability block diagram. START node on left initiates path from flight computer, into the system, ending with the base plate and other supporting structures.

2.7 Analysis Results

Running the models and calculating reliability values per the equations defined in section 2.4.5, ITEM toolkit generates tabulated results detailed in the following sections. A time of operation was defined as two hours, or the average flight test

Table 2.5: ITEM toolkit fault tree analysis results.

Parameter	Probability
Unavailability (Q)	0.094
Failure Frequency (ω_{sys})	0.046
CFI (λ)	0.051
Reliability (R)	0.963
FV Contribution	
Accelerometers	0.58
Fault Actuator	0.11
Thermocouples	0.10
Nominal Actuator	0.06
Load Actuator	0.05

duration for EMA fault injection experiments.

2.7.1 Fault Tree Analysis

The model suggests a high probability of reliable FLEA operation during a flight experiment. The analysis results from ITEM, shown in Tbl. 2.5, indicate that FLEA has over a 96% chance of operating as designed during the two hour test. However, there is a 5% chance FLEA experiences some sort of failure during the two hour window. It appears from the ranking of components via the Fussell-Vesely calculation that the components most likely to cause problems are the accelerometers, responsible for over half of the system unavailability. Comparing the percent contributions relative to the FMECA, the components do not necessarily match up with the highest risk numbers. This may be due to the bias within the FMECA and lack of failure data regarding the custom components.

2.7.2 Reliability Block Diagram Analysis

The second reliability model also suggests a high probability of experiment completion, as the analysis results indicate a 98% chance of reliable operation. Tbl. 2.6 presents the output from ITEM; FLEA appears to be a more reliable system according to this particular analysis. Furthermore, there is less than a 5% chance FLEA experiences a failure during testing. The Fussell-Vesely calculations also indicate the accelerometers contribute the most to system unavailability as a result of the long repair time and multiple installations. Checking with the FMECA, the one accelerometer does not have the highest risk, however when multiple are added together, then the FMECA begins to agree with the fault tree analysis. The high risk associated with the base plate and steel disk are not reflected with the analysis.

Table 2.6: ITEM toolkit reliability block diagram results.

Parameter	Probability
Unavailability (Q)	0.085
Failure Frequency (ω_{sys})	0.042
CFI (λ)	0.046
Reliability (R)	0.912
FV Contribution	
Accelerometers	0.62
Fault Actuator	0.12
Thermocouples	0.11
Nominal Actuator	0.07
Base Plate	0.04

2.8 Design Recommendations

The results presented here address critical component design and reliability analysis, and provide a dearth of design recommendations for building the next generation test stand that can more reliably generate quality actuator fault data sets and hence enable better actuator health monitoring. First, we acknowledge the fact that there is only one FLEA available for analysis, and that obtaining accurate component failure and repair rates is difficult; nevertheless, we believe that the reliability information was obtained from a legitimate source and used valid assumptions. Second, the standard FMECA was completed by the original FLEA designer and builder, which might introduce some bias; however, we believe that the designer was most intimately involved with the test stand, and hence is a reliable source for this information. And finally, the study was taken a step further by including fault tree and reliability block diagrams, albeit requiring stringent model assumptions; they produced meaningful results, at least from a mechanical point of view. Nevertheless, the validity of the model assumptions must be taken into consideration. The output is not coupled with a confidence level because the sample size is one, but that should not discredit the results. In fact, all of the assumptions expressed in section 2.4.4 do not hold over the life of FLEA; component failures do propagate through the system, failure rates do change over time, and as with any system with humans in the loop, ergodic trends will surface. But for a two hour flight time, the assumptions hold true. Therefore, the following FLEA design recommendations are given:

- Require CNC machining for all alignment sensitive components
- Design for quick repair of high risk components

- Secure FLEA components
- Increase actuator assembly work envelope
- Avoid the use of steel screws in aluminum plates
- Ensure FLEA enclosure is free of debris
- Add service loops and stress relief to all wiring within the test stand

2.8.1 Ensure Alignment

Referring to Tbls. 2.5 - 2.6, in order to reduce the actuator unavailability contribution, actuator alignment is one design aspect that could be changed. Flight surface control actuators are usually installed as two-force members, allowing for additional degrees of freedom as the controlled flight surface directs the flight surface. As a result, their alignment is constrained to a single plane. It is difficult to replicate this setup in a test environment because the actuators are coupled and de-coupled from their load; so the actuators must be constrained in all six degrees of freedom and hence their fixed alignment is of paramount importance. CNC machining is advised for the hole patterns on the base plate and the rigid bar because the remaining actuator assembly parts are installed relative to their location. To replicate the actuator environment and measure similar loading effects, this recommendation is critical to the quality of FLEAs fault data sets.

2.8.2 Design for Quick Repair of Critical Components

Each repair rate holds the assumption that the component being repaired is not immediately available and must be ordered, machined, installed and calibrated

like new. Having sensors and other high-risk electrical or mechanical components ready for installation is advised for quick turnaround. This practice would reduce the amount of accelerometer and thermocouple contribution to the system unavailability.

2.8.3 Secure FLEA components

The steel target disks should be secured with cotter pins or lock nuts and washers. Press fits or synthetic thread locks are also an option. The liberation of the steel disk within a high vibration environment is very likely, but nonetheless unacceptable. The actuators, sensors, linear rails, and the rigid bar should also be assembled with fasteners that contain lock nuts and/or lock washers to prevent them from coming loose during flight. It is worthy to note that increasing the flight time to four hours reduces system reliability to 85%. Knowing the models suggests that accelerometers contribute the majority of the reliability issues; design efforts should focus on more secure attachments, possible wireless applications, and good maintenance.

2.8.4 Increase Actuator Assembly Work Envelope

Introducing additional uncertainty in the vertical alignment of each actuator in the form of welded tabs is not advised; therefore increasing the size of the actuator assembly will remove the need for tabs in the first place. Doing so will promote accuracy in the installation and alignment of the actuators and increase the quality of the data sets. To further improve horizontal and vertical adjustment issues, a dedicated mounting bracket should be installed.

2.8.5 Avoid the Use of Steel Screws in Aluminum Plates

Screwing a steel fastener into an aluminum-threaded body will result in galling, regardless of the loading conditions. Stressing the fact that although, the base plate contributes a small amount to system unavailability during flight time, it should not be assumed that the threads are reliable. Steel fasteners should be used as through bolts with steel nuts and washers to secure the actuators and linear guide assembly. The FMECA risk priority number is the highest for the aluminum thread failure (448) and although the reliability models do not reflect this inference, a small design effort will eliminate this risk from affecting system reliability. Steel hardware will also allow for slotting of the aluminum plate and more adjustments available for alignment and installation of multiple actuators.

2.8.6 Ensure FLEA Enclosure is Free of Debris

Since the actuators casings have been opened to permit the installation of sensors. The seals that would ordinarily keep out debris have been rendered useless. To prevent actuator containments, the FLEA shell should keep out large particles. The addition of gasket material where the shell joins together will aid in the protection of the actuator lead screw assembly and prolong actuator availability.

2.8.7 Add Service Loops and Stress Relief to All Wiring

While it is not within the scope of this reliability study, it is worth noting that the wiring required to carry signals and power within FLEA needs to be considered airworthy and follow military specifications.

2.9 Conclusion

This paper has contributed to the development of quality EMA fault data through the analysis of critical component design and operation coupled with a reliability study of the FLEA itself over a two hour flight experiment. This study presented various analysis tools to help infer FLEA availability and individual component contributions to system reliability and the guarantee of quality fault data sets. The analysis shows FLEA to have 0.91-0.96 probability of reliable performance during testing. The results for the two analysis types agree with each other, indicating that the system was modeled correctly.

Using the design recommendations will be an essential part of the next generation FLEA, giving the designer the confidence that their implementation will produce a more reliable EMA test stand, and generate quality and robust actuator fault data sets.

Acknowledgments

This research is supported in part by the Air Force Office of Scientific Research under Grant Number AFOSR FA9550-08-1-0158. Any opinions or findings of this work are the responsibility of the authors, and do not necessarily reflect the views of the sponsors or collaborators.

Chapter 3 – Electromechanical Actuator Test Stand Coupling Design to Support Actuator Prognostic Model Development

3.1 Abstract

Uncertainty assessment and management is becoming an increasingly essential aspect of good prognostic design for engineering complex systems. Uncertainty surrounding diagnostics, loads, and fault progression models is very real and propagating this uncertainty from component-level health estimates to the system-level remains difficult at best. In this work, a test stand is used to conduct real-time failure experiments aboard various aircraft platforms to collect failure response data, expanding the actuator knowledge base that forms the foundation of component health estimations. The research takes a step towards standardizing a test stand design to produce comparable and scalable failure data sets, fostering uncertainty reduction within the electromechanical actuator prognostic model. This paper specifically presents a method to optimize the actuator coupling for a commercially available actuator where a model was built to minimize the coupling deflection and estimate the coupling life. Using this model, researchers can rapidly develop their own electromechanical actuator test stands.

Electromechanical Actuator Test Stand Coupling Design to Support Actuator Prognostic Model Development

Michael T. Koopmans¹, Graduate Research Assistant, koopmans@engr.orst.edu

Irem Y. Tumer¹, Associate Professor, irem.tumer@oregonstate.edu

¹Affiliation : Oregon State University, Corvallis, Oregon 97330, USA

**Proceedings of the ASME 2011 International Design Engineering Technical
Conferences & Computers and Information in Engineering Conference
IDETC/CIE 2011**

August 28-31, 2011, Washington, DC, USA

DETC2011-47869

3.2 Introduction

In an economy where large systems are becoming more complex and more plentiful, it becomes essential for real time information about the system to be available and useful. Complex system manufacturers have offered services of this nature for years [45, 46]. When a system health prediction is warranted, diagnostic technology is limited, whereas a prognostics architecture can be installed to infer this kind of knowledge. Most often referred to in the medical field, a prognosis offers patients a prediction of their future health. Within the engineering discipline, a prognosis may be defined as an extended prediction in time of a component or sub-systems' remaining useful life (RUL). Commonly modeled after a specific signal or fault indicator, the RUL metric is ideally presented in the form of a probability distribution function in terms of the model units (sliding distance, hours, missions, etc.) [5]. Depending on the model and amount of information available, the prediction carries with it a specific amount of uncertainty. Reducing this uncertainty is of paramount importance for several parties: 1) the designers who rely on the accuracy of the prognosis for their operation and maintenance schemes, 2) the users who query prognostic availability for real-time control, and 3) the managers who consult health statistics into their fleet management decisions.

Two recent aircraft accidents motivate and offer prime candidates for RUL modeling. One involves the extreme wear of a horizontal stabilizer trim actuator, where all aboard perished [11] and the other, excessive wear of the main engines, which resulted in the grounding of the entire fleet [47]. Effectively installed, a prognostics architecture may have been able to predict these failures given a valid model, confident diagnosis, and accurate previous usage history [48]. Yet, establishing a prognostics architecture in a complex system requires a great deal of prior

knowledge - not only about the prognostic model itself, but the economic need behind the development. The PHM community recognizes this problem: standard elements of prognostic research have been proposed [6] in addition to performance metrics to aid in the presentation and comparison of results [23]. In the case of large aircraft and spacecraft, implementing a prognostic solution is obvious, yet determining the optimal approach to characterize a diagnosis and its resulting prognosis, is extremely difficult. The choice is determined by many factors, e.g., application, sensor(s) available, ability to replicate operating conditions in accelerated aging experiments, RUL algorithm structure, and acceptable uncertainties. Of particular interest is the uncertainty management surrounding prognostic models, as several researchers from academia, industry, and government have shown in their work [49, 50, 51]. This paper seeks to address and foster uncertainty reduction through a standard approach to determine test stand design.

3.2.1 Paper Focus and Contributions

The typical prognostic model development path first chooses a test article, conducts failure experiments, captures wear progressions, and finally builds RUL algorithms in parallel with uncertainty assessment and management. The end goal is a prognostic architecture populated with several component models and the ability to propagate sub-system estimations to overall system health predictions with confidence. In many cases where failure data is needed to populate an RUL algorithm's knowledge database, a test stand is built and components are run to failure. Here, the experimental design and operations can directly affect the correlation between the actual failure relationship and the relationship captured on the test stand. By standardizing and methodically determining a test stand design,

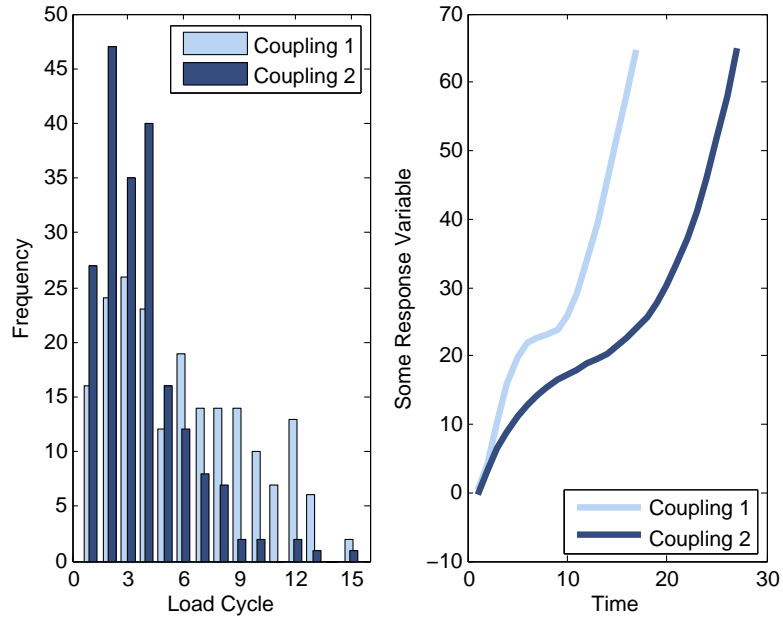


Figure 3.1: An example comparison of two couplings with their load occurrence on the left and corresponding wear variable response on the right.

we can judge the validity of the failure data used in developing a prognostic model [52]. As an example, consider Fig. 3.1 where two different couplings are shown with their corresponding loads and resulting actuator response wear variable (e.g., temperature, vibration, hysteresis). In this example, coupling no. 1 has a higher percentage of higher loads because the mechanical flexibility in the coupling exacerbates the problems the control scheme has with following its intended path. As a consequence, the wear variable quickly reaches a certain threshold, most likely not representing the underlying wear relationship the experiment is seeking. On the other hand, coupling no. 2 is what the wear relationship that was measured using an optimized coupling may represent. By carefully taking into consideration the loading and layout, a stiffer coupling allows for better load profile following, isolating the fault to failure progression, and thus allowing a more accurate representative wear model to be captured. Not optimizing the coupling of a test stand

conducting failure experiments may contaminate the data sets and eventually increase uncertainty in the prognosis. This problem affects the actuator prognostic model by associating a load profile with a wear model that may not be possible in the real system.

Therefore, this paper presents a method to optimize a coupling for in-flight actuator failure experiments. The design objective is to produce a coupling that remains stiff during experiments while maximizing structural integrity for the duration of test stand operations. This work contributes an optimization method for deriving an actuator coupling design using geometry, material property, operating condition, and other constraints. Beginning with a background of actuator test stands and sources of prognostic uncertainty, an approach is developed given a commercially available electromechanical actuator, experimental loads, materials, and layout to produce a coupling design suited for reliable use in an experimental test stand.

3.3 Background

Electromechanical actuator (EMA) technology is steadily improving and their benefits over traditional hydraulic and the newer electrohydrostatic actuators are real [18, 14, 12]. Researchers have begun to study the failure effects of EMAs in an effort to test the robustness and reliability relative to the other actuators, should they be used as replacements [9, 28]. Particularly, the Prognostics Center of Excellence at NASA Ames Research Center [53] has recognized that, in order to accelerate the adoption of EMAs in aircraft, their fault to failure propagations should be captured and classified [26, 27]. Most recently, an in-flight experimental test stand has flown aboard multiple military platforms with promising results [8]. Fig. 3.2 shows the

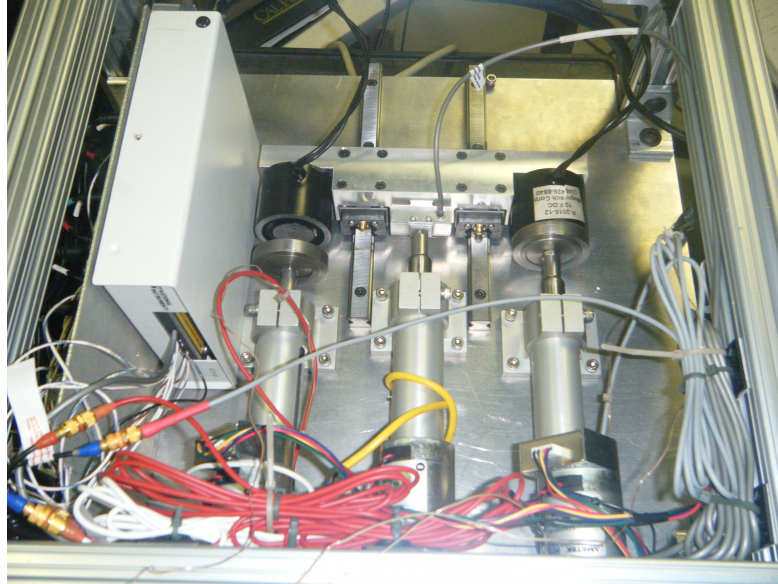


Figure 3.2: A top view of the actuator coupling currently installed on the FLEA [1].

actuators and coupling inside this test stand, named FLEA, where several sensors monitor the actuators' response. The usefulness of the data captured aims to spark a trend towards more testing, with more test stands, and more actuators. With more test stands, a standard design should be proposed and validated so as not to introduce any confounding variables into the data sets [1]. Thus, the accelerated failure data sets can be preserved for comparison between data sets from other test stands and be confidently swapped between different prognostics models.

3.3.1 Uncertainty in Design and Prognostics

Regardless of what method is used, there will be uncertainty in the prognostic models. Successfully assessing and propagating this uncertainty through the design of complex systems is convoluted [54] and even if the sub-system RUL estimates are available, actually implementing a complete prognostics solution within a complex

system design is a very difficult task [21, 22, 55]. Hence, if a prognostics and health management (PHM) framework is to be relied upon, its mathematical foundation must be rigorously developed and tested. This stage of development though, brings the argument and question of how to specify, design for, and ultimately validate the prognosis. One such domain where the clarity of requirements and engineering specifications cannot be ignored is in the design of military systems. Research is underway to develop an enterprise-wide health management framework to solve this problem [29, 56]. Yet, PHM still finds it difficult to gain traction within the government and industry due to uncertainties surrounding its integration at many levels. In response, program managers were advised at a PHM 2010 conference panel session to fund development of PHM technology [57] in place of a deliverable, e.g., one less end item.

Several aspects contribute to the uncertainty of prognostic models and their resulting RUL estimations. At a high level, the entities that contribute to uncertainty are shown in Fig. 3.3, where three main components (current state, future load profile, and damage progression models) piece together the overall prognostic model. Each of these components have associated uncertainties that may propagate to other parts of the model and so it is important that the design of experiments considers the requirements for the prognostic model. This in turn will reduce uncertainty associated with the component/sub-system prognostic models, ultimately increasing the confidence of the system prognosis.

Typically the largest source of prognosis uncertainty is that associated with the damage progression model. One area that was known to be rushed during the FLEA design was the coupling, where, during particularly intense use, the total deflections may exceed 5 mm. The effect is difficult to observe in the data sets, but extraordinary wear may be occurring that is not relative to position or force,

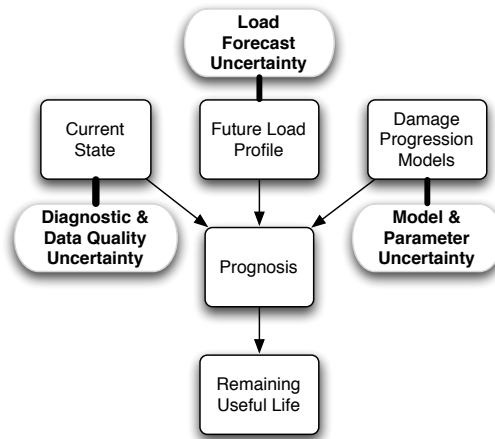


Figure 3.3: A high level prognostic model [2].

yielding inaccurate model development.

3.3.2 Model Uncertainty

Model choice for PHM applications is an involved process where several approaches (physics-based, data-driven, or hybrid) may be taken to accurately model component RUL, which is most often a nonlinear relationship. Each model that is chosen incurs a level of model uncertainty - as is the result of using simplified mathematical relationships in place of the physical relationships occurring within the system [58]. In order to quantify the uncertainty, a model is first defined as being composed of two parts: its structure and parameters. The model's structural uncertainty sources can be found in geometry, initial and boundary conditions, assumptions, data, among others. Parameter uncertainty is more straightforward as it resides in the actual confidence limits of the parameter values themselves, whereas the calculation of structural uncertainty is difficult to fully assess and propagate, yet it often contributes the most to model uncertainty [59]. Thus, by optimizing and

proposing a standard actuator coupling, uncertainty between the data sets, and thus prognostic models, may be reduced.

3.3.3 Load Uncertainty

Another source of uncertainty in the prognostic model is that associated with the future load profile. Load uncertainty refers to the distribution of information known by the prognostic model regarding the future load profile representation in the near and extended time scales [2]. A battery model for instance, may have known statistical parameters as to what its discharge load will be whereas a bearing model may have a set of loads coupled with a set of rotational velocities. In our case, an actuator model may have a set of load profiles for specific missions aboard different aircraft. For example, a cargo supply mission will contain takeoff, enroute maneuvers, and landing. The actuator prognostic model for this mission may assume a nominal mission profile with a corresponding response [60]. Where, the load uncertainty is realized during takeoff or landing when the pilot input is more or less aggressive, resulting in a different response. Uncertainty assessment and management dilemmas occur elsewhere in helicopter transmissions [61], batteries [62], crack growth [63], and chemical interactions [64].

3.3.4 Actuator Application

Assessing and managing uncertainty for actuator prognostic models installed aboard large aircraft is still several years off, but the current approach of fielding test stands to run experiments is a good intermediate step. Apart from lab tests, the in-flight experimental test stand is capable of monitoring actuators in real-time

while imposing scaled down loads derived from the dynamic pressure and attack angles of a given flight surface. Specifically, the load is calculated and imposed via a load actuator that is rigidly coupled to the test actuator(s). Several aspects of the test stand design affect the load transfer between actuators - the control algorithms, load calculations, and the coupling itself. Mechanically, the coupling offers a prime candidate for a design optimization problem given the prognostic goal and test articles. In addition, solving the actuator coupling problem can improve reliability of the test stand [65], facilitate future actuator research projects, and possibly decrease uncertainty within actuator prognostic models.

3.4 Overview of the Approach

The following section describes the general approach for designing an in-flight actuator coupling. This approach will attempt to guarantee the structural integrity of the coupling for the duration of the test stand operations and indirectly support quality actuator prognostic model development. Beginning with the experimental objectives and scope, the test articles, coupling layout, and optimization model development are described next. The input to the model is actuator specifications and their loading conditions. The optimization yields dimensions for a suggested coupling with estimated deflections and cycles to failure. This approach is intended for the researcher who wants to build a test stand of their own, populate their failure model database, and generally continue discussion within the PHM community as to what constitutes standard tests for determining actuator RUL.

Step 1: Define experimental goals and assumptions. The overall goal of a test stand is to operate in an environment that closely resembles its future in-

stallation and capture real time nominal and failure actuator response. The first step will aim to set requirements and specifications that guarantee precise load following during operations and data capture. It is important here to remember that the data captured can be used to test 1) online diagnostic and prognostic algorithms, 2) offline RUL models, and, 3) uncertainty assessment and management tools. The data set's ability to scale up to larger actuators will depend on many factors: loading conditions, environmental exposure, and sensors available. Beginning with a thorough conceptual design, the derivation of achievable requirements will specify allotted volume and mass in addition to actuator sample size and science obtainable.

Step 2: Identify test articles and procedures. In this step, the purpose is to identify and choose test articles that either are the exact actuator to be used in system operation or a scaled-down version because the test actuator's failures will be characterized during the experiment. It is important that the architecture (i.e., electric motor, gearbox, linear screw drive, ball nut) be similar, so that when a model is constructed for the system actuator, the model scales up well. Linear actuators will be the primary test articles for this study, but hydraulic actuators could be used if they possess similar end attachments. Typically installed as a two-force member, the linear actuator experiences routine loads during commercial aircraft operations with a low probability of non-routine maneuvers. On other military and government aircraft, the actuator's load is somewhat stochastic, forcing the load estimate to be uncertain. Regardless, the conditions surrounding the actuator load depend highly on the aggressiveness of the control, possibly more than the application or operating environment. Initially, the optimization model will assume the maximum potential load supported by the coupling is $\sqrt{2}$ times

the maximum operating load value. Consequently, knowing the load profile will allow for a comparison with the calculated cycles to failure.

Step 3: Design the coupling layout. Given the chosen actuators and test procedure, the next step is to design a coupling to transfer the load in a representative path similar to system operation (e.g., flight surface control). The model choice for the layout is made given a specific number of actuators (load and test) from experimental goals. Ideally, the data acquisition system should monitor both a nominal and faulty response under almost identical operating conditions. This is an important assumption and design decision. The researcher will benefit by obtaining a response for both faulted and nominal actuator responses similar in almost every aspect, except for the injected fault itself. Manufacturability, assembly, and sensor access should be taken in consideration when refining the layout as well. Only then can design variables be identified and materials suggested.

Step 4: Develop optimization model. Based upon the design variables and coupling layout, the next step is to build a generic optimization model customized to the test stand. The designer will tailor the model to minimize overall coupling deflection while satisfying strict fatigue scenarios. This goal will attempt to determine a level of certainty that the coupling will not affect test actuator response. Deflection of the coupling will be represented by an objective function of the form $\min f = y(\mathbf{x})$, where \mathbf{x} represents the set of design variables, and f represents total coupling deflection. Several constraints in the form of design, stress, mass, and fatigue will then be applied to the model. Five different constraints will be used in the optimization: upper and lower bounds (e.g., $x_1 \geq X_1$), linear equalities (e.g., $x_1 + x_2 = C_1$), linear inequalities (e.g., $x_1 - 2x_2 \leq C_2$), nonlinear equalities (e.g.,

$x_3^2 + x_4 = C_3$), and nonlinear inequalities (e.g., $x_1^3 - x_2^2 \leq C_4$), where generally speaking, x_i represents some design variable and C_i represents some constraint constant.

Step 5: Perform optimization. Once the coupling geometry, objective function, and constraints have been specified, the optimization is performed. First, a monotonicity analysis is completed to verify that the design variables are well-constrained. Understanding these relationships will help the engineer better understand the model. The flow of information starts with a solver running some flavor of a minimization process, operating with the set of design variables, \mathbf{x} , while satisfying the constraints, $c(\mathbf{x})$. The model is completed with the integration of the force and position profiles. If the profiles are not available, estimate reasonable ones.

Step 6: Analyze the Results. The final step is the output of the optimization model. With information on coupling deflection relative to arm length, design variable values, the solid model, and a life estimate, the engineer has several options. The solid model may be used for finite element analysis to verify structural integrity and/or stiffness while the life estimate can be compared against the load cycling found within the first few characteristic experiments. From here, the engineer designs an arm & shaft fastening solution in parallel with the integration of the remaining test stand equipment.

3.5 Demonstration / Numerical Example

In this section, a demonstration is presented to optimize a coupling for use in an experimental EMA failure test stand. Two couplings will be designed for two

different sets of test articles. The results are presented next following the steps detailed in the previous section.

Step 1: The experiment. For this case study, it will be assumed that the test stand objectives are in parallel with the previously designed flyable actuator test stand currently in operation [8]. It will be flying aboard similar aircraft while obtaining real-time flight information in order to calculate actuator loads and positions. For proper bias in the experimental data, the test stand will incorporate two test actuators (one nominal, one faulted) and a load actuator. The sensor suite will be comprised of a load cell for use in actuator force control, accelerometers located on the test actuator's ball screw, and thermocouples located on the test actuator's motor. Other sensors include motor current, potentiometer, and rotary encoders. In order to properly maintain these sensors, especially the ball nut accelerometer, access within the test stand must be available (these requirements will be embodied in the constraints). Previous experience suggests that the coupling mass be approximately 2 kilograms. Also, a volume envelope set at 700 mm length, 150 mm wide, and 250 mm depth is not to be exceeded.

Step 2: The test articles and procedures. The test articles the coupling will be designed for are the Ultra Motion Bug [66] and the Moog model 973 [67] actuators. These actuators were chosen for demonstration because of their size and design relevance to larger actuators. They both have similar strokes, force output, and velocity capabilities. Assuming three actuators will be contained in the test stand, the load actuator does not have to be the same as the test actuators, but is advised for control and integration purposes. The two test actuators are mostly identical except for their proposed fault injections (determined by which failure

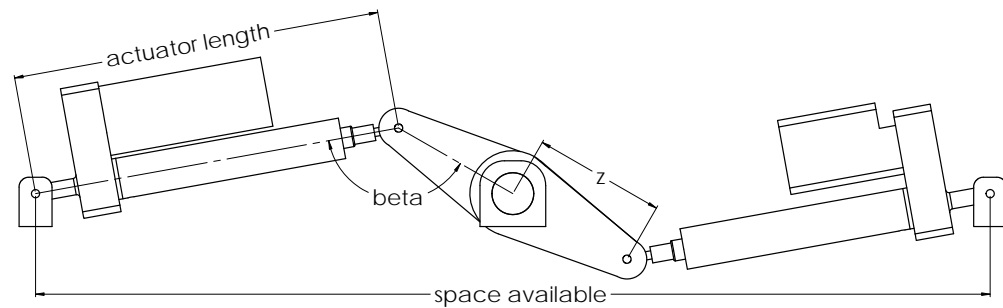


Figure 3.4: Coupling layout showing design values used in the optimization.

modes the experiment will test).

The first failure modes tested were a return channel jam and a lead screw spall with promising results [8]. The test procedures will coincide with flight operations, during which, the aerodynamic loads on the actuator of interest are calculated using dynamic pressure and attack angle from the flight sensors in addition to the wing geometry. From previous tests, the maximum operating load was around 315 N and the future experiments will be of similar magnitude. So a maximum potential force of 445 N was used in the optimization model. The test actuators will be controlled via a position loop where maneuvers from the pilot in the form of pitch control determine the actuator extension. Therefore the load and test actuators (controlled by different loops) will aggressively search for equilibrium while being rigidly coupled and highly dependent on each other.

Step 3: The coupling layout. Taking an influence from pivots and constrained motion techniques found in most flight surface control methods, the load and test actuators will face opposite each other while the coupling layout will be centered around a rotating shaft with extension arms. A side view of the solid model layout is shown in Fig. 3.4. On the left is the load actuator (larger motor), while

on the right is the test actuator. The other test actuator is stowed in a neutral position when it is not coupled. To describe the figure labels, *actuator length* is variable with a maximum of 386 mm and a minimum of 285 mm, *space available* is a pre-specified allotment of space (700 mm), z is the arm length, and *beta* is the angle between the actuator centerline and the arm centerline. The last two parameters become important within the optimization model because they are varied to search for the highest loading conditions. The load actuator is coupled to a test actuator at all times as test actuators switch during experiments to capture both nominal and faulted responses. The coupling is designed to be flexible for different sized actuators, easily built, and simple to operate. The main components of the coupling include the stepped shaft shown in Fig. 3.5 where a single piece of bar stock is turned to different diameters estimated by the optimization model, then specified by the engineer (ensuring press fits & standard bearings sizes are met). The length of the shaft is defined as $l = 2(AD + DE + 1.5b + GH)$ where b is the width of the mating surface between the shaft and arms, AD is a set bearing length, DE is variable with a minimum of 10 mm, and GH controls the amount of space allotted for sensor access. The arm is assumed to be a rectangular beam with width b , height $h_i = \frac{d_i}{2} + 23$, and variable length. Here the constant 23 mm represents a built-in value for averaging the height at the shaft center relative to the center of the actuator end connection. Retaining rings and keyways may aide the press fit of the arm onto the shaft, preventing it from rotating about the shaft axis. The coupling layout attempts to follow manufacturing and assembly design principles.

During optimization analysis, the loading condition (symmetrical about the shaft center, I) is assumed to be where a test actuator holds a fixed position. The force variables F_t & F_r represent the tangential & radial force components,

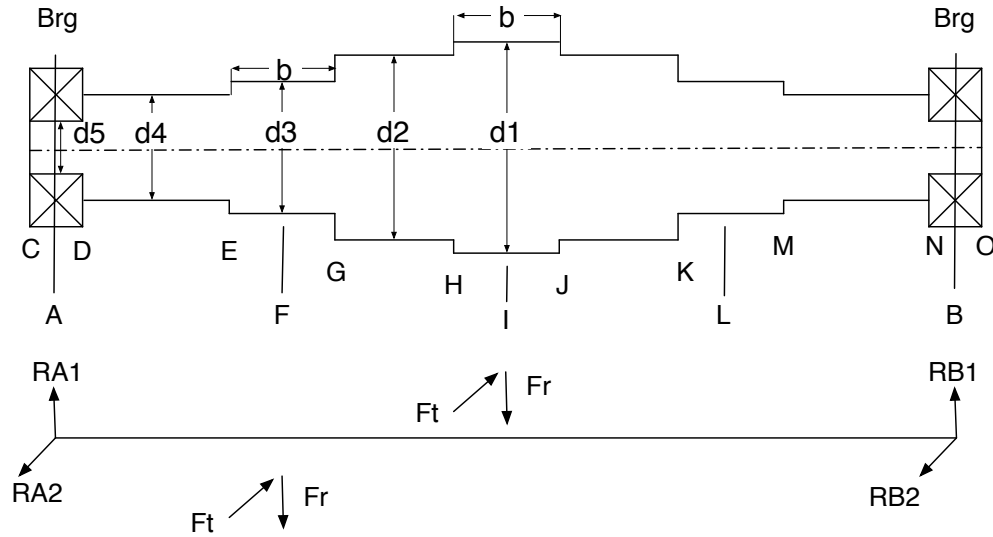


Figure 3.5: Cross section view of the coupling shaft with applied and reaction force components.

respectively, of the total force from the load actuator (F), applied relative to angle β . Points of interest for sizing diameters should be shoulders (e.g., stress at H will size d_2), particularly G and H because they experience the highest moments and torque in the stepped shaft. Closed-form analysis will assume A and B are pin supports, while the maximum shaft length and mass are set to 152 mm and 2 kg, respectively. These values are based on engineering judgment and may be adjusted to satisfy variable requirements. Therefore, the following design variables have been specified: b , GH , d_1 , d_2 , d_3 , d_4 , and d_5 , where each is assigned to the set of design variables, \mathbf{x} (i.e., $b = x_1$, $GH = x_2$, etc.). Materials being considered for the coupling include 6061-T6 Aluminum and 1020 mild carbon steel.

Step 4: The model. Given the above layout and design variables, an optimization model to minimize coupling deflection can be built. First, the coupling geometry is solved, material properties are loaded, and force estimations are set. Next, the objective function is formed to calculate the coupling deflection, followed

by constraint estimation. To reiterate, the deflection of the coupling is of particular interest because its minimization will provide a rigid support structure for testing the actuators, where the resulting load following control is specifically designed to be more accurate. To achieve a closed-form solution for the coupling deflection, it must be broken into two parts: the rotating shaft and extension arms. The following derivations can be found in [68]. End deflection of the arm is modeled in Eqn. 3.1.

$$y_{\text{arm}}(\mathbf{x}) = \frac{F_t}{F_r k} (\tan kz - kz) \quad (3.1)$$

where $k = \sqrt{\frac{F_r}{EI_a}}$, $I_a = \frac{bh_1^3}{12}$, $h_1 = \frac{d_1}{2} + 23$, and z represents arm length. Again, the constant 23 is a built-in value for averaging the height relative to the actuator connection. At the arm and shaft mating surface (width = b), the design variable h_1 and h_3 have the same relationship with their respective mating diameters, d_1 and d_3 . The second half of the objective function is the shaft deflection, modeled with Eqn. 3.2.

$$y_{\text{shaft}}(\mathbf{x}) = \frac{2Fa}{6EI_s l} (2l - a)(l - a)x_p + \frac{\sqrt{R_{A1}^2 + R_{A2}^2}}{6EI_s} x_p^3 - \frac{2F}{6EI_s} (x_p - a)^3 \quad (3.2)$$

where a is the point along the shaft axis at which the force is assumed to be imposed, E is the modulus of elasticity of the shaft material, $I_s = \frac{\pi d_s^4}{64}$ (or found in a lookup table derived from I_s values in the solid model), d_s is the effective shaft diameter, l is the shaft length, and x_p is the point at which the deflection is being measured. These two deflections are added together, yielding the objective function shown in Eqn. 3.3.

$$\min f = y_{\text{shaft}}(\mathbf{x}) + y_{\text{arm}}(\mathbf{x}) \quad (3.3)$$

This objective function will estimate the total mechanical deflection of the coupling at the fastener interface with the actuators. Indirectly, it also yields the slope along the shaft axis which may be used for bearing selection. Points of interest for x_p would be the shaft center and any shaft shoulders. For the first estimate, it was found that the highest deflection would occur at the center of the shaft after completing the shear and moment diagrams.

Next, the optimization model constraints are described. First, lower bounds were placed on the design variables to specify minimum values of $b \geq 15$ and $GH \geq 5$. The bounded constraints ensure a minimum amount of material is in place on the arm for the clevis connectors. Second, the linear relationships constrain spacing for sensor access, diameter reductions, and maximum shaft length as shown below in Eqns. 3.4-3.5:

$$c_1 = -b - GH \leq -\frac{s}{2} \quad (3.4)$$

$$1.5b + GH = \frac{l_{\max}}{2} - AD - DE \quad (3.5)$$

where s is equal to the width of an actuator plus 7mm for adequate user access and l_{\max} is the longest allowable shaft length. The maximum length has been divided by two in Eqn. 3.5 because of loading symmetry and consequently, geometry symmetry. The remaining diameters are set relative to each other for standard shoulder heights: $1.1d_3 \leq d_2 \leq 1.25d_3$, $1.1d_4 \leq d_3 \leq 1.25d_4$, and $1.1d_5 \leq d_4 \leq 1.25d_5$. Third, the nonlinear relationships limit fatigue failure criteria at various points of interest with high stresses and geometry reductions in addition to a maximum coupling mass. A maximum safety factor will constrain d_2 and d_3 as seen in Eqn. 3.6. The stress derivations can be found in [69].

$$c_2, c_3 = nf_{\max} \geq \frac{S_e S_{ut}}{\sigma'_a S_{ut} + \sigma'_m S_e} \quad (3.6)$$

where S_e is the endurance limit ($S_e = k_a k_b k_e S'_e$), S'_e is the test specimen endurance limit, and its k factors are calculated using the surface ($k_a = 2.7 \frac{S_{ut}}{1000}^{-0.265}$), size ($k_b = 0.91 d_2^{-0.157}$), and reliability ($k_e = 0.814$) values. The safety factor is set to a maximum as typical parts with small deflections will have large safety factors. Here the safety factor has been set to a range between two and four based on previous experience with coupling design and the uncertainty about imposing loads. The alternating stress is represented in Eqn. 3.7.

$$\sigma'_a = \sqrt{\frac{32K_f M_a^2}{\pi d_2^3} + 3 \frac{16K_{fs} T_a^2}{\pi d_2^3}} \quad (3.7)$$

where the stress concentration factors where K_f and K_{fs} are derived from their static counterparts K_t and K_{ts} , and M_a plus T_a are the alternating moment and torque. For the mid-range stress (σ'_m), M_m plus T_m are used as taken from the moment and shear diagrams. The mass of the coupling is constrained using Eqn. 3.8 below.

$$c_4 = m_c \leq 3x_1 x_3 z \rho + \pi r_s^2 l \rho \quad (3.8)$$

where the mass of the arms is taken from their dimensions: width b , length z , and height h . The mass of the shaft is calculated using its effective shaft diameter d_s (the average of the shaft diameters respectively weighted to their percentage of total shaft length). Once the coupling mass has been limited (2 kg), the set of constraints is complete and ready for implementation.

Step 5: Optimization. Here, the constraints, objective function, coupling geometry, and actuator specification come together to form the complete optimization model. Any software package with an optimization solver will suffice for implementation, particularly one that accepts nonlinear constraints. This work has

been implemented in MATLAB, using the solver contained in the function `fmincon` and verified with the built-in genetic algorithm `ga`. Before solving the model, a monotonicity analysis is completed to ensure the model is well-constrained (shown in Tbl. 3.1). Each relationship on the left denotes its effect on the optimization by

Table 3.1: Monotonicity Analysis.

Relationship	Design Variable						
	b	GH	d_1	d_2	d_3	d_4	d_5
y_{arm}	-		-		-		
y_{shaft}	-	-	-	-	-	-	-
c_1	+	+					
c_2	-	-		+			
c_3	-		-			+	
c_4	+		+	+	+	+	+

holding a lower bound (-) or upper bound (+) on their respective design variables. For example, the objective function components at the top of the table, show a lower bound is held with y_{arm} on b , d_1 , and d_3 . In addition, y_{shaft} holds upper bounds on b and GH and lower bounds on all five diameters. The remaining relationships c_1 through c_4 complete the monotonicity analysis; indicating that each design variable has either a lower bound when increasing or upper bound when decreasing. To clarify, when c_4 is active, it constrains d_1 , d_3 , d_4 , and d_5 , assuming c_2 constrains d_2 . Further, depending on the status of the optimization, c_2 or c_3 will be active. Therefore, this optimization model is well-constrained by the first monotonicity principle [70]. The block diagram in Fig. 3.6 shows the flow of information through the optimization model. The `main` function loads the actuator specifications, coupling material, and arm length, pushing it to the `optimize` function. The solver minimizes the `objective` function while satisfying the set of

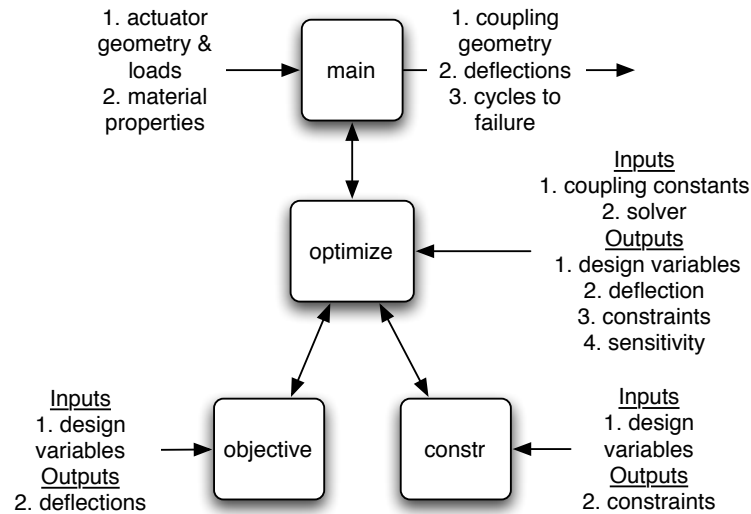


Figure 3.6: The optimization model architecture.

constraints. Ten different arm lengths between 76 mm and 120 mm were applied in the optimization process while global variables were used in the model to pass material properties and geometric constants.

Step 6: Analysis of results. The coupling design has been optimized using the design variable set \mathbf{x} , constraint set $c(\mathbf{x})$, and objective function f . This section first presents total coupling deflection relative to arm length, followed by a chosen coupling design, and ending with life estimates. The top level of the optimization model parses through several different arm lengths and optimizes at each step, giving the engineer many options in terms of actuation envelopes. Fig. 3.7 shows the arm length options for the two materials. The plot shows that at a 100 mm arm length, both material couplings are estimated to have the same deflection, while before and after, the deflection does not vary by more than 25% between materials. Overall, the deflection is never more than 0.04 mm. This is an acceptable value considering previous couplings had displacements of more than 5 mm. The

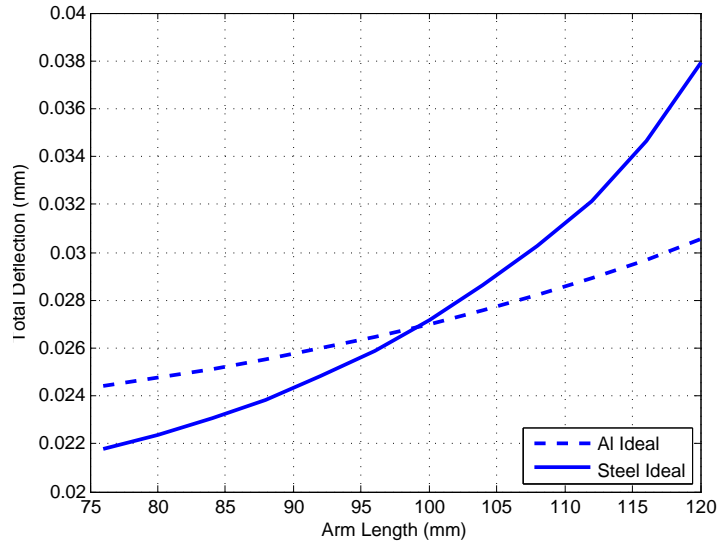


Figure 3.7: Deflection plot for both materials.

decision then depends on how the material will interact with other components of the test stand (e.g., will magnets be used to couple and de-couple the two test actuators? Will heli-coils be required for aluminum threads?) Nevertheless, a stiff coupling design will positively influence the control scheme within the flyable test stand, and consequently, the failure data produced. The effect of the constraints is evident as the steel coupling deflection becomes larger. For a more detailed look at how the variables change with the arm length, Fig. 3.8 and Fig. 3.9 show the results for the aluminum and steel design variables, respectively, where b and GH initially diverge, then remain constant and match the diameter's behavior. A similar relationship exists for the steel coupling except b and GH diverge in the opposite direction throughout to account for the mass constraint. The aluminum coupling never reaches the fully allotted mass of 2 kg, while the steel coupling mass is always 2 kg. For further analysis, a coupling with an arm length of 100 mm will be chosen. The design values for this coupling can be seen in Tbl. 3.2. Here, the

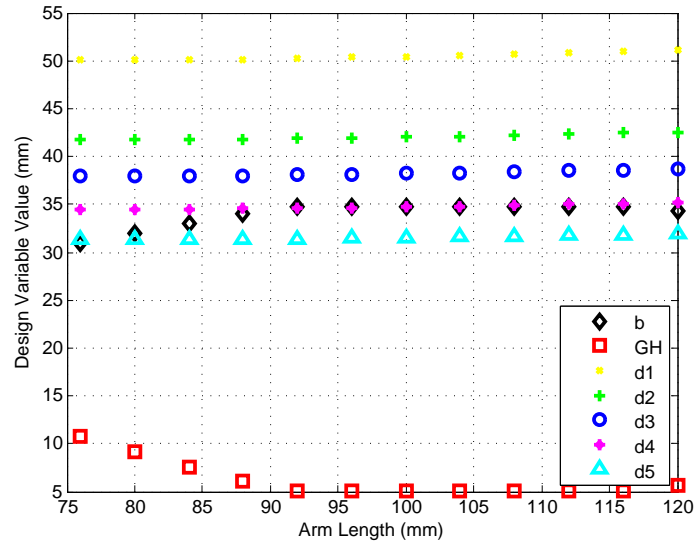


Figure 3.8: 6061-T6 Aluminum design variables.

Table 3.2: Optimization results for 100 mm arm length.

Material	Design Variable							unit
	b	GH	d_1	d_2	d_3	d_4	d_5	
6061-T6	34.7	5.0	50.4	42.0	38.2	34.7	31.5	mm
+5 %	6.3	0.7	-6.0	-1.1	-6.3	-2.2	-1.0	%
1020 steel	11.6	39.7	39.9	33.2	30.2	27.5	25.0	mm
+5 %	0.4	4.7	-3.7	-2.9	-1.8	-1.8	-1.1	%

variables are presented along with their effect on the total deflection (originally 0.027 mm) if they were perturbed an additional five percent. Although very small, no design variable perturbation results in a change of total deflection by more than seven percent - a verification of the coupling stiffness. The behavior indicates that as the coupling length was increased (b and GH), the shaft deflection rose, while as the coupling diameters were increased, the shaft deflection lessened (a stiffer shaft & higher arm moment of inertia). These design variables can be input directly

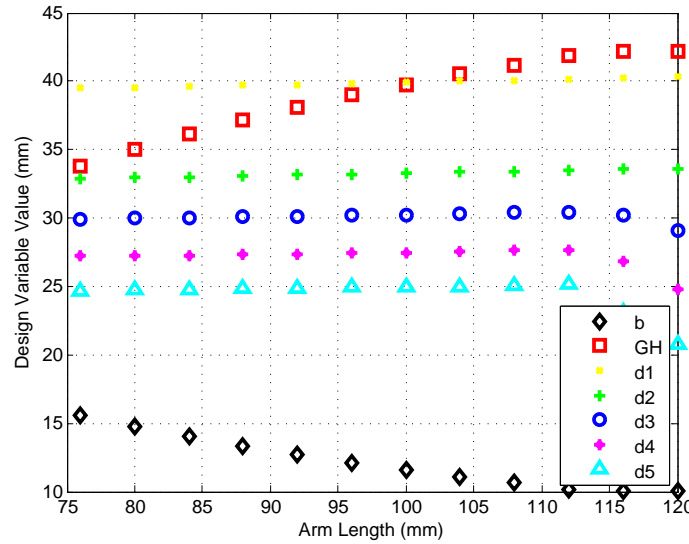


Figure 3.9: 1020 mild steel design variables.

into a solid modeling program. Solidworks was utilized here, as shown in Fig. 3.10 for both test actuators coupled.

Next, the number of cycles until failure can be estimated using Eqn. 3.9.

$$N = \left(\frac{S_f}{a}\right)^{\frac{1}{b}} \quad (3.9)$$

where, $S_f = \frac{\sigma_a}{1 - \frac{\sigma_m}{S_{ut}}}$, $a = \frac{(0.9S_{ut})^2}{S_e}$, and $b = -\frac{1}{3} \log\left(\frac{0.9S_{ut}}{S_e}\right)$. This calculation assumes fully reversed loading (which is very conservative) and a failure indicating material yielding. It is important to note that this is an initial estimate that will change when the exact loading conditions are known. And so, taking the previous comments into consideration, the steel coupling has an estimated life twice that of aluminum; specifically, 8000 cycles compared to approximately 4000. Depending on the actuator placement aboard the aircraft, the length of a cycle could be long (possibly once or twice per flight), or less (around 100). From here, coupling design can be integrated with the rest of the test stand equipment - sensors, data

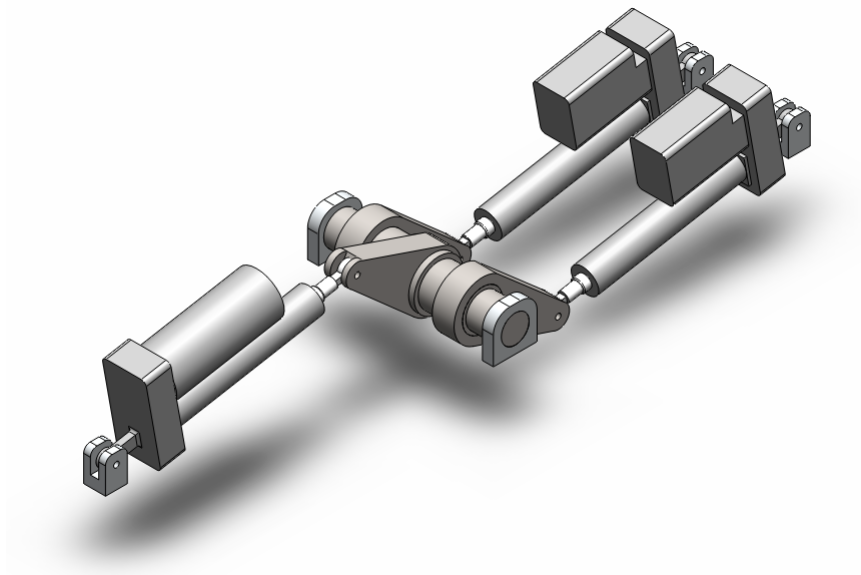


Figure 3.10: Optimized actuator coupling solid model.

acquisition, signal conditioning, and control systems.

3.6 Discussion

An optimization of a coupling for in-flight failure experiments has been presented. The goal of this work was to contribute a model and method to derive a standard actuator coupling for one load actuator and two test actuators using geometry, material property, operating condition, and other constraints. Outlining the method and presenting the results for a given actuator yields several observations:

1. Prognostics and health management research is an expensive journey and by design, usually results in extremely dependent findings. This is unavoidable because of the large number of assumptions behind research efforts, especially when testing components to failure. In the case of electromechanical

actuators, a goal of having a large knowledge base of fault to failure damage progression responses (ideally scraped of sensor and ambient noises) is not far off. Pulling information from these knowledge bases to model the damage of an actuator would become commonplace, where techniques would be developed to negotiate the differences between the actual response and the actuator attempting to be modeled (geometry, loads, application, faults, sensors available, etc.). Therefore, designing failure experiments with very few confounding variables is good practice and this is where the optimization model makes a contribution: by aiding the back end of a project (design) while positively influencing the front end (RUL modeling).

2. The application of the optimization model is specific to the actuator geometry, loads, and coupling layout. For a coupling design with a different set of actuators or layout all together, the same design principles can be applied. Assuming the actuators possess two clevis connections is also important to the model, as other actuator installations may include pivots or even a second linkage. Having one load actuator and two load actuators is the most economical and best choice for capturing data sets relative to nominal and faulted cases almost simultaneously.
3. Designing a test stand coupling that multiple researchers can use in their experiments enables collaboration, making the task of sharing and comparing their results easier. This work supports the effort to standardize an aspect of actuator prognostic research with the goal of creating an atmosphere similar to that found in the medical field, where standard research methods such as the double blind study have been used for decades.
4. Although this research is directed towards achieving high confidence data

sets for actuator prognostic models, the technology can be applied anywhere actuators are employed. One obstacle in monitoring the actuator response elsewhere is the available sensor suite in the system of interest. The benefit of the optimized coupling here is that the response captured by the sensors is relative to the current state of the actuator (faults, force, length, environment) and little else, so transferring the current sensor's response given a known set of actuator variables is possible to another domain (e.g., manufacturing robots where a current sensor is likely one of the few sensors installed).

3.7 Conclusion

In this paper, a coupling for a flyable EMA test stand was optimized to propose a standard design for a specific failure experiment actuator layout. The model has shown to produce an extremely stiff coupling given the constraints and an estimated several thousand cycle life. With a stiff coupling, the actuator's load profile following ability improves, focusing more energy to the actuators, and eliminating a set of test stand design and operation dependencies when developing the actuator prognostic model. Future work for this research will incorporate analysis of actual failure experiments aboard the FLEA and their uncertainty quantification, in addition to the development of new test stands.

Acknowledgment

This research was supported in part by the Air Force Office of Scientific Research under Grant Number AFOSR FA9550-08-1-0158 and was started at the NASA Ames Research Center. Any opinions or findings of this work are the responsi-

bility of the authors, and do not necessarily reflect the views of the sponsors or collaborators.

Chapter 4 – Wave Energy Converter Bearing Health Estimation and Experimental Test Stand Benchmarking

4.1 Abstract

Ocean waves can provide a renewable and secure energy supply to coastal residents around the world. This paper presents the application of a PHM based research methodology to derive empirical models for estimating the wear of polymer bearings installed on wave energy converters. Forming the foundation of the approach is an applicable wave model, sample data set, and experimental test stand to impose loading conditions similar to that expected in real seas. The resulting wear rates were found to be linear and stable, enabling coarse health estimations of the hypothetical bearing surface. The work presented here is an initial investigation of a larger, more comprehensive reliability assessment for wave energy devices.

Wave Energy Converter Bearing Health Estimation and Experimental Test Stand Benchmarking

Michael T. Koopmans¹, Graduate Research Assistant, koopmans@engr.orst.edu

Stephen Meicke¹, Graduate Research Assistant, meickes@onid.orst.edu

Irem Y. Tumer¹, Associate Professor, irem.tumer@oregonstate.edu

Robert Paasch¹, Associate Professor, paasch@engr.oregonstate.edu

¹Affiliation : Oregon State University, Corvallis, Oregon 97330, USA

International Journal of Prognostics and Health Management Society

Submitted July 2011

4.2 Introduction

Aggressive development of new energy resources for an ever growing human population is currently underway, and ocean waves have shown promise as a viable source of renewable energy. The interest in offshore power production is due in no small part to the proximity of consumers: over the next 15 years, 75% of the world's population is projected to live within 200 km of the coast [71], while the worldwide resource has been conservatively estimated to contain 200 - 500 GW of economically extractable energy [72]. Yet, designing, installing, operating, and maintaining systems to harness this renewable energy is an extremely complex problem from multiple standpoints. From an engineer's perspective, the most immediate and challenging problems revolve around device reliability and survivability within the marine environment.

Located in extremely energetic wave climates, a wave energy converter (WEC) is subjected to an array of loads and millions of oscillatory cycles per year. Depending on the device, certain components will degrade more rapidly than others, particularly the bearing surfaces that many WEC designs rely upon. Here, prognostics and health management (PHM) techniques and research methods can be applied to help predict levels of degradation. Often times, the quality of the bearing surface directly affects the total cost of the device in terms not limited to 1) power take-off efficiency, 2) scheduled and/or non-scheduled maintenance, and 3) device survivability. It is therefore apparent that the success of research efforts to assess and manage WEC reliability remains a critical step to the growth of the ocean renewable energy market.

The PHM system health research methods have proven fruitful for years [5] and are sought to aide in WEC component-level experiments. A WEC's complexity, al-

though not as involved as an aircraft, automobile, or submarine, is intensified with its naturally corrosive, brutal, and immense spectrum of marine operating conditions. Therefore, extensive and efficient use of laboratory experiments is needed to build the marine renewable community's database of seawater based component life models. To populate this database, an accepted and scalable methodology is needed. This paper consults a proposed PHM research methodology [6] to lay the foundation for an experimental approach to measure bearing wear. More specifically, this study aims to assess the wear characteristics of polymer-based bearings immersed in seawater that are subject to loads and oscillations similar to those experienced by a point absorber WEC in real seas. Our investigation has three goals:

1. Verify and benchmark test stand design and operation for bearing wear measurements
2. Conduct wave energy research following a proposed PHM methodology
3. Present an initial study of polymer bearing health estimation utilizing wear models derived from a set of generalized representative sea states

4.2.1 Main Contributions of the Paper

The work presented here is the beginning of a larger research effort to assess and manage WEC reliability, maintainability, and overall system health using PHM based techniques. Beginning with the bearing design and operating effects, accurate material wear models are a critical factor in determining the efficiency of the device power output. The contributions of this study are itemized as follows:

- Utilization of a PHM based methodology to determine polymer bearing wear models with respect to their pressure and velocity parameters in seawater
- Wave climate load classification was detailed for a point absorber WEC in generalized real seas
- Cumulative wear of proposed bearing material was estimated for a given month
- Relevant information provided to ocean renewable developers and partners so it may help them assess the applicability of the materials and improve the technology
- An experimental test stand's performance was benchmarked and recommendations were offered for future bearing tests

4.2.2 Roadmap

The paper will begin with a brief background section including an introduction to the point absorber WEC, application assumptions, and an overview of the PHM research method consulted. Next, the wave climate and the process used to determine experimental wave cases is discussed, followed by a description of the experimental setup. Results of the bearing wear tests, their implications, and future studies are also presented.

4.3 Background

This section will provide a brief description of the chosen wave energy converter (WEC), test stand effects, and modeling considerations. To begin, there are gen-



Figure 4.1: Oscillating wave energy converter devices.

erally four main groups of WEC designs: oscillating water columns, overtopping devices, point absorbers, and attenuators (Fig. 4.1) [73, 74, 75]. Each device relies on bearings to either support a turbine shaft (water columns and overtopping) or provide a sliding surface on which two large masses can move relative to each other [76]. Specifically, the point absorber and attenuator WECs are designed to harvest the heave motion of a passing wave through their power take-off (linearly or rotationally), where the relative motion of two or more large masses is exploited to generate electricity. Other examples of seawater exposed bearing applications include wind plus wave energy harvesters [77] and sea floor based rotational power take-offs [78].

4.3.1 The Point Absorber

Focusing on the point absorber design, the system contains a few core subsystems: power take-off, mooring, structures, control, and distribution (Fig. 4.2). The device

is capable of translating in three degrees: heave (up/down), surge (forward/back), sway (starboard/port) and rotating three degrees about its axis: pitch, yaw, and roll. This investigation will only consider the structures subsystem of a point absorber WEC (buoy and spar) and its heave dynamics relative to the sea state. Power take-off, mooring, and control do play very important roles in the loading conditions of the bearing surface, albeit require much more knowledge about the WEC system itself that is not covered in this paper. Essentially, this study assumes one degree of freedom (heave) and a float that is a perfect wave follower. In other words, when solving for the heave dynamics, it will be assumed that as each wave passes, the buoy will travel up and down with the water surface. This relative velocity between buoy and spar is the exact velocity the bearing surface will experience during operation (i.e., power generation). In storms however, the WEC is most likely not converting energy and may switch to a survivability mode; one possible technique locks the buoy in place to prevent system damage. The

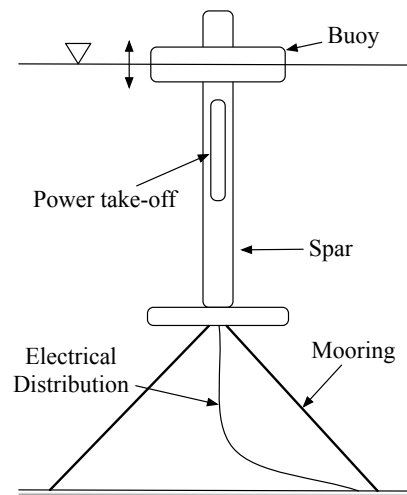


Figure 4.2: A generic linear power take-off point absorber WEC architecture layout, where relative motion between the buoy and spar provide energy conversion opportunities.

bearing subsystem is integrated into the structure of the WEC and provides a surface on which the buoy and spar may move relative to each other. To avoid installing a bearing material sleeve along the entire inner diameter of the buoy, one possible solution lays two to four equally-spaced counterface extrusions around the spar, where they are mated with bearing blocks impregnated within the buoy. Here, the bearing requirements for many WEC technologies demand the surface to be inexpensive, corrosion-resistant, low maintenance, and near-zero friction in a large variety of loading conditions. One proposed solution utilizes a polymer-based approach, similar to those found in current naval designs [79] and hydropower applications [80, 81].

This simple polymer-based approach has proven to be beneficial in such applications for its ability to self-lubricate and deposit a transfer film on the counterface, filling in surface asperities, linearizing the wear rate, and even reducing friction in some cases [82]. However, water's tendency of inhibiting or wholly preventing transfer film formation is a research topic itself and will only be indirectly addressed in this work. Research regarding wear characterization of polymer journal bearings has been published at various pressures, velocities, and environmental conditions [83, 84]; yet, few studies have been shared with the wave energy community presenting the results of seawater immersion [85, 86], let alone under pressures and velocities expected to be experienced by WECs [87]. So, with an immature technology being relied upon by a large complex system, an experimental test stand has been designed and used to gain essential knowledge about the bearing material's performance characteristics under representative loading conditions.

4.3.2 PHM Based Techniques

Previously mentioned, the research methodology born in the PHM community provides a good platform on which test stand research can be integrated into a larger, more comprehensive effort to assess system health. A general outline is shown in Fig. 4.3, where the path to implementing and relying upon a prognostic solution begins with high-level system requirements (health predictions for subsystems and / or the system itself) that define the subsequent metric, fault, and sensor selection process. Next, the third step determines the most appropriate approach in terms

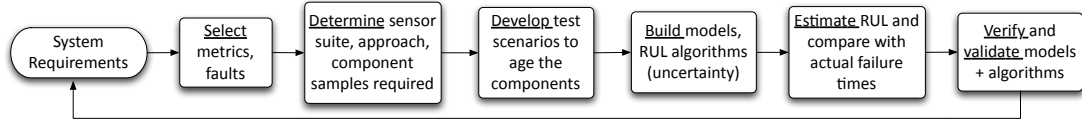


Figure 4.3: A universal PHM research methodology.

of desired performance, available resources, and acceptable uncertainty to satisfy the component-level predictions. Here the proper number of samples to sacrifice for an accurate inference is also set. The fourth step ascertains the test scenarios, design of experiments, testing, and data collection, while the fifth step is dedicated to building models and remaining useful life algorithms for nominal and faulted conditions. The last two steps encompass the health estimation and actual usage comparisons, in addition to the verification and validation sequences. A good application of the entire PHM research methodology estimated battery capacitance over time using high quality test chambers [7]. For this work however, only a few steps of the methodology are addressed for estimating WEC bearing wear. Knowing that it would be useful to predict bearing wear in extreme marine conditions, the initial approach to determine adequate experimental conditions and data collection procedures is described in addition to how the test stand itself contributes to the main goals of this investigation.

4.3.3 Test Stand Considerations

The test stand design and operation is critical to the validity of the empirical bearing wear models. Many interested researchers have built test stands to measure the degradation of particular components including batteries [49], actuators [8, 28], and polymer bearings [88]. The particular test stand employed for the experiments presented in this paper is a modified version of American Society for Testing and Materials' (ASTM) standard test for ranking plastic resistance [89], where the major changes to the standard include an oscillatory velocity, varying loads, and immersing the sample in seawater. Being a relatively new field of research, a lack of verification and validation of the modified test stand contributes to the uncertainty of the results. A goal of this work is to verify and benchmark test stand design and operation, ensuring the bearing wear measured repeatedly and accurately reflects imposed loading conditions.

4.3.4 Modeling Considerations

When investigating and modeling polymer bearing wear, it is important to note that multiple factors contribute to the wear rate. A polymer bearing / counter-face tribosystem failure modes and effects analysis may contain only a few failure causes, where a primary failure would be the direct result of the physical amount of bearing material removed, and secondary failures may be attributed to biofouling or sediment-rich seawater. This study only covers the primary failure (wear) and does not address secondary failures. Also, a wear estimation is considered synonymous with a bearing health estimation because the bearing's ability to perform as designed is assumed to be directly attributed to the physical amount of material remaining.

We must also consider the naturally stochastic ocean waves. Their modeling effort has been well documented [90, 91, 92] and the trade-off between the relevance of a higher fidelity numerical model and a closed-form solution must be done. For this work, the mapping of sea state to bearing pressure and velocity will be solved analytically with several conservative assumptions (e.g., linear waves, buoy / spar dynamics) that serve well as an initial attempt to assess the applicability of this research.

4.4 The Wave Climate

Within the fourth step of the PHM methodology, expected sea states are sought to derive the pressures and velocities experienced by the bearing surface. In order to choose experimental cases representative of WEC oscillations and loads, a wave climate comparable to permitted sites was chosen [93]. A wave climate is defined here as the comprehensive aggregation of all the reported wave measurements taken at a specific location. The most accessible sources for past wave climate information include the Coastal Data Information Program [94] and the National Data Buoy Center [95] who manages a worldwide buoy network. A buoy of particular interest for its similarities to a potential WEC installation (proximity to coast / large population areas, consistent and predictable wave energy) is located 15.5 nautical miles northwest of Winchester Bay, Oregon (NDBC station ID: 46229), where the water depth is 186 meters and the buoy is assumed to be a perfect wave follower.

4.4.1 Wave Data

Wave information is often reported in the frequency domain as a wave spectrum, where for each frequency and respective bandwidth, the energy or wave energy density is registered [96]. Other parameters included in the report can denote the wave direction, depending on the buoy. Much more wave data is also available apart from the spectral information including the raw time series values, which is of use for much higher fidelity WEC modeling. For the purpose of this study however, only two parameters were used in defining the wave climate: significant wave height (H_s) and dominant wave period (T_D). The significant wave height (in meters) is the average of the highest one-third of all the wave heights encountered during the 20 minute sampling period. The dominant wave period (in seconds) is the period with maximum wave energy as taken from the wave spectrum over the sampling period [97].

4.4.2 The Sample Data Set

Significant wave heights and dominant wave periods were taken for years 2005 - 2010 [95]. Reporting data every hour until the end of January 2008, the sampling rate was increased to every half hour. The entire dataset is not complete, as some data points are erroneous (e.g., $H_s = T_D = 99$) or absent altogether. To include some of these reports in the sample dataset, the erroneous points were replaced with the average of their nearest neighbors, whereas the absent points were left out of the averaging process. No weighting was installed to unbias the months with more hours reported over the months with lesser hours reported. There were four major gaps in the data, where no reports were given for the following dates: 1/1/05

4.4.3 Choosing Experimental Cases

In order to effectively achieve a spread of experimental cases, the wave period distribution was analyzed as shown in Fig. 4.5 while the wave heights were taken at each period interval. An interval is defined here as a particular one second period bin determined by the average and standard deviation of the cumulative wave period distribution where the column of wave heights is then sampled to find the exact experimental case (i.e., H and T). For the test period of 10.89 sec, the 10 - 11 sec period bin was analyzed (Fig. 4.6), as were the other three test period bins (7 - 8 sec, 13 - 14 sec, and 16 - 17 sec) to achieve all four experimental cases (Tbl. 4.1).

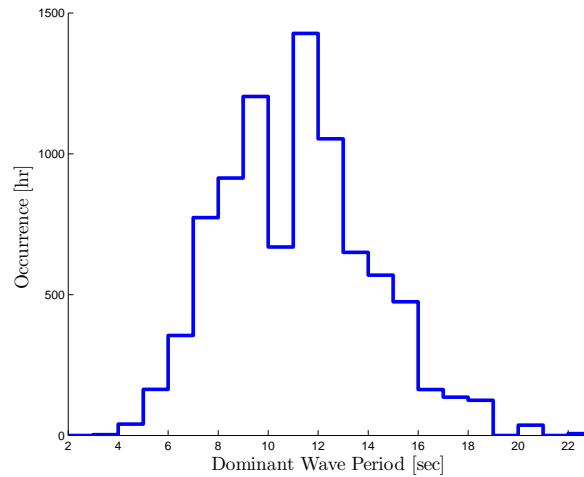


Figure 4.5: Wave period distribution over the entire climate data set, with an average of 10.89 sec and a standard deviation of 2.95 sec.

4.5 Experimental Design

This section will explain the design decisions and limitations behind the bearing wear experiments and their corresponding parameters, including the bearing

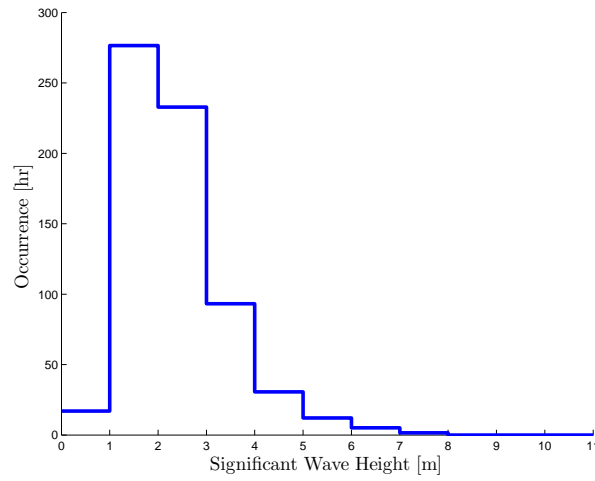


Figure 4.6: Distributions of significant wave heights for the 10 -11 sec period bin with an average of 2.3 m and a standard deviation of 1.0 m.

Table 4.1: Chosen test wave heights and periods.

Exp. Case	T(s)	H(m)
1	10.89	2.31
2	13.84	5.51
3	16.79	2.92
4	7.95	1.74

health estimation algorithm - addressing step three and parts of step five of the PHM methodology. Knowing the experimental wave parameters, the calculation of pressures and velocities at the surface of interest is described. First, a description of the procedure to compute the loading condition input for each bearing wear experiment is presented, followed by a table containing each experimental case parameter. Many assumptions support the closed-form approach taken in this paper and will be discussed as they are applied.

4.5.1 Wave Modeling and Force Calculation

First, the wave experienced by the WEC is classified using four main parameters: water depth h , wave height H , wave length L , and wave period T (Fig. 4.7), where η describes the wave surface elevation in terms of x and t while having a value of z meters. The wave itself is assumed to be harmonic and linear (or regular);

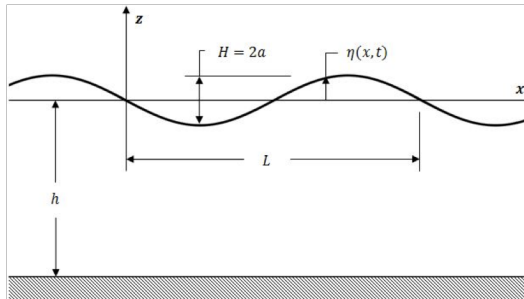


Figure 4.7: A regular two dimensional wave with relevant parameters and coordinate system shown.

other wave classifications include irregular, ocean, and stochastic ocean waves [98]. Generalizing the sea state under linear wave theory is the most basic approach to modeling the ocean surface and is deemed appropriate for this initial study.

The generalization assumes the fluid to be incompressible and inviscid (irrotational), enabling the local water particle velocities to be explicitly solved and

facilitating the use of Morison's equation [99]. In a typical design, a software program is tasked with computing the structural loading (e.g., AQWA, WAMIT). However, in our case, the Morison equation will be shown as an initial approach to calculate bearing pressure.

Next, assuming an intermediate water depth, the wave length is solved numerically using Eq. 4.1, where g is the acceleration due to gravity. A water depth of 91.4 meters was used in this study to mimic Oregon sites where large WEC developers currently hold permits [93].

$$L = \frac{g}{2\pi} T^2 \tanh \frac{2\pi h}{L} \quad (4.1)$$

The wave length can be verified for use in an intermediate water depth by checking the inequality (Eq. 4.2), where the wave number is $k = \frac{2\pi}{L}$. When calculating a kh scalar towards the lower or upper extremes, a shallow or deep water assumption, respectively, would instead prove more accurate.

$$\frac{\pi}{10} < kh < \pi \quad (4.2)$$

Next, the water surface displacement, η , is given in Eq. 4.3, where $\sigma = \frac{2\pi}{T}$ and its correlated velocity potential, ϕ , is given in Eq. 4.4.

$$\eta(x, t) = \frac{H}{2} \cos(kx - \sigma t) \quad (4.3)$$

$$\phi = -\frac{gH}{2\sigma} \frac{\cosh k(h+z)}{\cosh kh} \sin(kx - \sigma t) \quad (4.4)$$

The closed-form velocity potential allows for the calculation of horizontal ($-\frac{\partial\phi}{\partial x}$) and vertical ($-\frac{\partial\phi}{\partial z}$) water particle velocities, which can be seen in Eq. 4.5 and Eq. 4.6, respectively.

$$u = -\frac{\partial\phi}{\partial x} = \frac{gHk}{2\sigma} \frac{\cosh k(h+z)}{\cosh kh} \cos(kx - \sigma t) \quad (4.5)$$

$$\nu = -\frac{\partial\phi}{\partial z} = \frac{H\sigma}{2} \frac{\sinh k(h+z)}{\sinh kh} \sin(kx - \sigma t) \quad (4.6)$$

The local horizontal acceleration is shown in Eq. 4.7.

$$\frac{\partial u}{\partial t} = \frac{H\sigma^2}{2} \frac{\cosh k(h+z)}{\sinh kh} \sin(kx - \sigma t) \quad (4.7)$$

Using these equations, an estimation of the horizontal force imposed on the buoy by a passing wave can be computed.

Typically used to design and estimate loads on columns embedded in the sea floor, Morison's equation (Eq. 4.8) can be extremely useful during conceptual WEC design for computing the horizontal wave force imparted on the device by a passing regular wave [100]. The equation is composed of two elements, the first captures the drag forces and the second captures the inertial forces,

$$F(z) = \frac{1}{2}C_D\rho Du|u| + C_M\rho V \frac{Du}{Dt} \quad (4.8)$$

where C_D , C_M , ρ , D , and V represent the drag & inertial coefficients, seawater density ($1025 \frac{\text{kg}}{\text{m}^3}$), buoy diameter, and buoy volume. Ultimately integrated over a water depth with respect to z , total horizontal force is represented in Eq. 4.9,

$$F_x = \int_a^b F(z) dz \quad (4.9)$$

where b is usually the water displacement(η), and a is some value in the vertical length (z) of the geometry. For example, if $a = -h$, the force would integrate over a continuous column to the sea floor. The aggregation of Eqs. 4.3 - 4.9 can be

viewed in Fig. 4.8 and Fig. 4.9, where the parameters of a $H = 3\text{ m}$, $T = 12\text{ sec}$ wave are plotted implementing the zero crossing method.

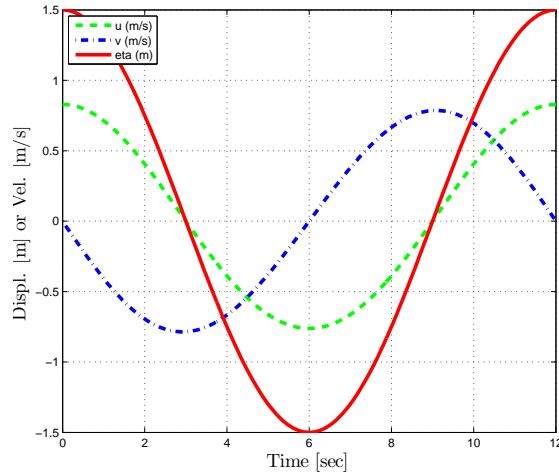


Figure 4.8: Example surface displacement and corresponding water particle velocities for a $H = 3\text{ m}$, $T = 12\text{ sec}$ wave.

4.5.2 Experimental Case Parameters

Incorporating the above wave model, chosen wave heights and periods, and force calculations, the experiment case parameters can now be set (Tbl. 4.2). To reiterate, the experimental cases are a first attempt at a sample set of representative wave parameters to classify polymer bearing wear during WEC operation. The third column states the maximum velocity the counterface experiences during the oscillatory profile (i.e., Eq. 4.6). Next, geometric assumptions that enable a specific velocity and pressure to be applied during wear tests are held and explained as follows. A buoy diameter of 11 m was used in the Morison force calculation while the force was integrated over a depth of 1.5 m. This depth was chosen based off the assumed buoy height (1.5 m) and assuming the buoy was fully submerged throughout the length of the passing wave. Next, knowing linear wave theory was

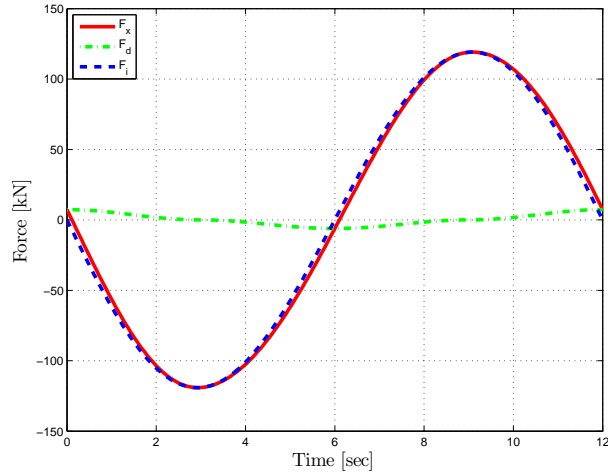


Figure 4.9: Example force oscillation imposed on the buoy by a passing $H = 3$ m, $T = 12$ sec wave, where F_d and F_i represent the individual components of F_x : the drag and inertial forces, respectively. The actual normal force applied to bearing sample was taken as the root mean squared value of the maximum F_x due to test stand limitations.

Table 4.2: Experiment Case Parameters

Exp. Case	T (s)	H (m)	ν_{\max} (m/s)	F_{rms} (kN)	P (kPa)	kh
1	10.89	2.31	0.66	78	334	3.1
2	13.84	5.51	1.25	120	500	2.0
3	16.79	2.92	0.55	47	202	1.4
4	7.95	1.74	0.69	108	445	5.8

being utilized, the drag and inertial coefficients were taken as 1.3 and 2.0, respectively [101]. The bearing pressure was computed using the wave force calculation and an assumed bearing area of 0.232 m². This particular area was chosen as a conservative estimate of the total bearing area and set the active bearing pressure below the bearing manufacturer's recommendations.

The final parameter set for the wear testing experiments was the number of runs for each experiment case. Using the operating characteristic (OC) curve to minimize the type II error, Eq. 4.3 was implemented [102],

$$\Phi^2 = \frac{nD^2}{2a\sigma^2} \quad (4.10)$$

where Φ and β (probability of type II error) make up the OC curve x and y parameters. Further, n is the number of runs for each test climate, D is the difference between two treatment means desired to be detected (0.5), a is the number of experimental cases (4), and σ is the assumed maximum standard deviation of wear rate at any power level (0.1). These values were based on previous wear studies completed. Tbl. 4.3 shows the results of checking various sample sizes and it was decided due to the infancy of this research that a probability of 0.85 would be adequate for detecting a difference in wear means (D) for separate experiment cases. Consequently, three test runs were specified for each experimental case.

4.5.3 Bearing Health Estimation

Once the bearing wear experiments have concluded, the post-processing of the raw linear variable differential transformer (LVDT) measurements should ideally indicate a linear and stable wear rate. Under these circumstances, the wear models

Table 4.3: Determining each experimental case's sample size using the operational characteristic curves with $\alpha = 0.01$.

n	Φ^2	Φ	$a(n - 1)$	β	Power ($1 - \beta$)
2	6.3	2.5	4	0.5	0.5
3	9.3	3.0	8	0.15	0.85
4	12.5	3.5	12	0.01	0.99

can be pieced together to create a cumulative data driven life model of the bearing surface. This inference allows ocean renewable developers the capability to predict the bearing's health after some length of time. For example, if the life model indicates the amount of bearing material lost is approaching a critical threshold, then operators and maintainers can make informed decisions. Given enough time, the repairs could be scheduled to minimize the cost associated with servicing the bearings. It is important to note that the prediction accuracy of the bearing health estimation can be directly attributed to wear model quality and its associated experimental design.

In order to quantify the raw bearing wear in a format applicable to wear predictions, the recorded vertical wear from the LVDT is multiplied by the constant contact area to form the total volumetric wear for the sample seen in Eq. 4.11,

$$V = 2wrq \sin^{-1}\left(\frac{l}{2r}\right) \quad (4.11)$$

where w is the vertical wear, r is the counterface outer radius, l is the sample length, and q is the sample width (all variables in mm). To avoid biasing the wear estimate to focus on force or distance or time alone, a specific wear rate variable is used (Eq. 4.12),

$$V = eFs \quad (4.12)$$

where V is the total volumetric wear (mm^3), e is the specific wear rate ($\frac{\text{mm}^3}{\text{Nm}}$), F is the normal load (N), and s is the sliding distance (m). Solving for e using the stable portion of the wear plot, a set of specific wear rates are then available to the user for calculating volumetric wear of the bearing during different climates than those tested in the experiment. Assuming the worst case scenario for the specific wear rate model formulation, forces and sliding distances are then derived for each particular hour of reported wave parameters. The cumulative volumetric bearing wear is tracked using Eq. 4.13,

$$\sum_{i=0}^n V_i c_i \quad (4.13)$$

where i is the bin index (wave height and period), V is the volumetric wear associated with a particular bin and c is the total number of hours the WEC experienced seas classified to the particular bin. This purely data driven model would preferably be used in parallel with the wave climate in Fig. 4.4 and although relatively elementary, could be enormously useful in estimating the overall bearing health, while further informing WEC design, operation, and maintenance decisions.

4.6 Experimental Setup

This section will describe the bearing material and its mating counterface used during this study - addressing step four of the PHM methodology. The test stand is also shown and the procedure to measure bearing wear is described.

4.6.1 Bearing Material

Each bearing sample was machined out of disks (with an inner radius equal to the counterface) 6.40 mm in width into sections of 15.85 mm in length and approxi-

mately 10 mm in height. The Thordon SXL bearing material was used throughout the study [103]. Each bearing sample was cleaned with methanol prior to each test to guard against any incidental debris from contaminating the experiment.

4.6.2 Counterface

Two identical 316 stainless steel counterfaces were used during testing, each with a diameter of 63.5 mm (derived from the rpm limit of the motor so as to maximize the range of test surface velocities) as seen in Fig. 4.10. Before and after each test run, the surface roughness of the counterface was measured using a Mitutoyo surface roughness tester in an attempt to determine any transfer of material to the counterface. As per design recommendations from the manufacturer, the counterface surface roughness was made to be less than $0.8 \mu\text{m Ra}$ before each test. In an effort to allow for better mechanical bonding of the polymer, roughening was completed perpendicular to the direction of rotation [104]. The roughness measurements were taken in parallel to the direction of rotation at three different points along the width of the counterface and six different section widths around the circle. Prior to each test, the counterface was also thoroughly cleaned with methanol.

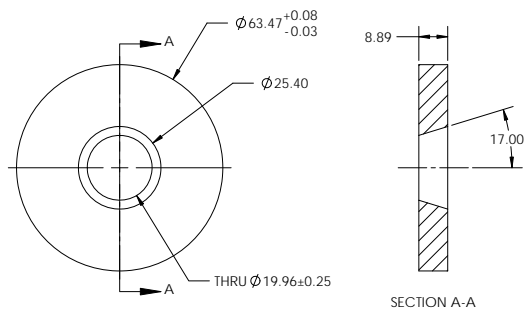


Figure 4.10: Counterface dimensions.

4.6.3 Test Stand

Using a testing method derived from the ASTM G176-03 standard [89] for ranking wear resistance of plastic bearings, the test stand can be seen in Fig. 4.11. Modifications to the setup have been made to allow for complete immersion of both the bearing sample and counterface in seawater. A procedure to run a bearing wear test follows:

1. Empty all seawater from reservoir and wash out with freshwater, lightly touching the counterface (remove salt, but not the transferred bearing material) and remove bearing sample.
2. Remove the counterface from drive shaft, air dry, and measure surface roughness.
3. Take the second, prepped counterface and couple to drive shaft, ensuring minimum change in deflection of the surface during rotation. The authors recommend using a dial indicator to measure this deflection.
4. Set the new, prepped bearing material in place, load mass on vertical shaft, latch front plate, fill reservoir, input test parameters to software, and begin test.

The removable counterface is held in place with two plastic nuts on a stainless steel drive shaft directly coupled to a DC brushed motor. A 0.5 μm resolution LVDT was tasked with measuring the vertical wear of the bearing sample while linked to the vertical shaft responsible for holding the mass load in place. The drive shaft and all connecting parts were cleaned with methanol prior to each test. The seawater used during testing is seawater filtered to 50 μm , taken from Yaquina Bay in Newport, Oregon.

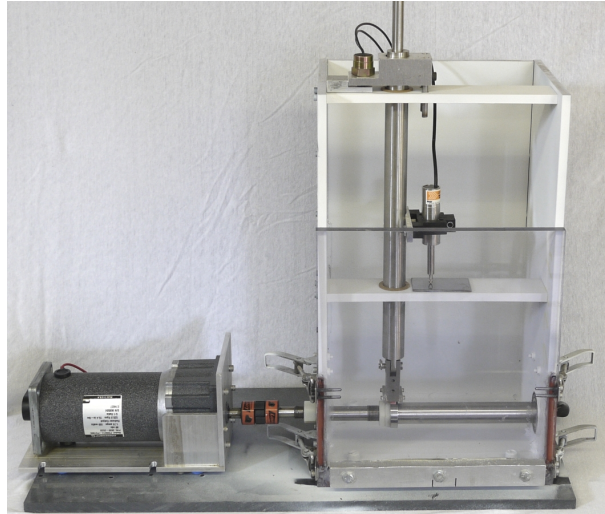


Figure 4.11: The bearing wear test stand.

A National Instruments cRIO unit was programmed to control motor velocity using the LabVIEW interface and shaft encoder relaying speed information. The bearing samples were subjected to sinusoidal velocity profiles (ν) oscillating at their specified frequency ($\frac{1}{T}$) and each wear test was run for 20 hours with no intermittent stops. In order to determine the correct mass to load the sample, the test climate pressure (P) was multiplied by the bearing sample projected area and divided by the gravity constant, g .

4.7 Results

This section will present the results of all twelve wear tests, grouped into their four respective experiment cases, followed by the specific wear rate model formulation, a month long bearing health estimation, and the corresponding before and after counterface surface roughness measurements. The raw LVDT readout was smoothed for graphing purposes. Each wear plot contains two x-axes: sliding distance (computed from oscillation frequency, amplitude, and counterface radius)

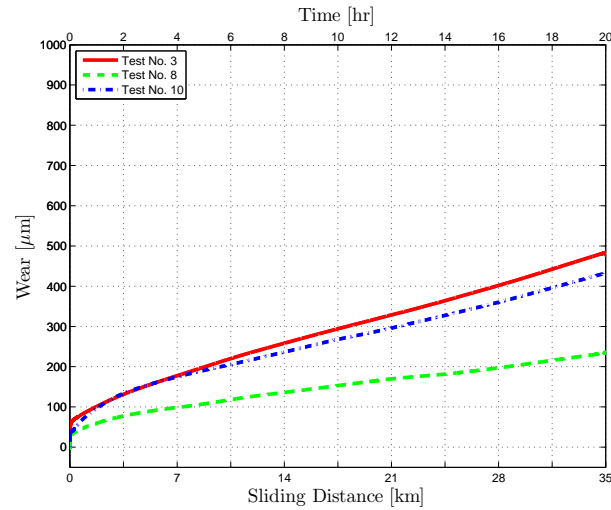


Figure 4.12: Experiment case one, pressure = 334 kPa, maximum surface velocity = 0.66 m/s, mass = 3.382 kg.

and time (each wear test was 20 hours long). The first case is shown in Fig. 4.12, while the second, third, and fourth cases are shown in Figs. 4.13 - 4.15, respectively. General intuition is correct as the plots show the highest pressure resulted in the highest wear rate, while the lowest pressure resulted in the lowest wear rate. And for the majority of test runs, similar patterns exist within each experimental case. However, test run number twelve is an anomaly: around hour seven, the wear measurement diverges and increases 350% less than the previous two test runs. Another test run that is unlike its counterparts is number eight, where its wear measurements are offset 50 - 100% less than test run three and ten.

Next, ensuring wear was linear with respect to time and distance, hour six to twenty was set as the stable portion of the wear plot for all test runs. Analyzing this segment, a vertical bearing wear measurement can be used to derive the total volumetric wear and specific wear rate for each test run. Here the results can be seen in Fig. 4.16, where the dotted line represents a worst case scenario specific wear rate model. For a month long wear estimation, the specific wear rate model was

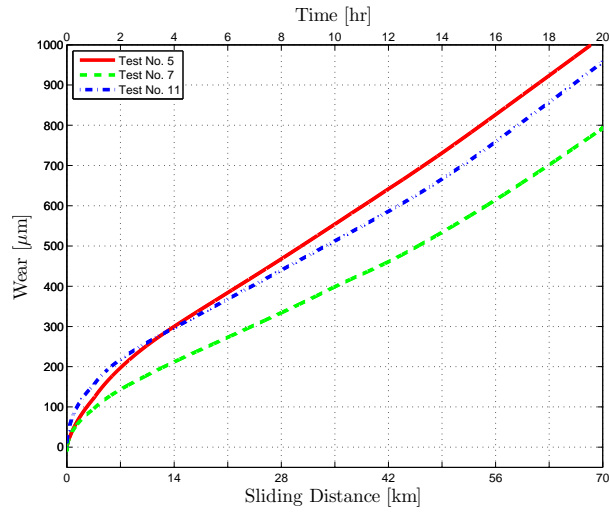


Figure 4.13: Experiment case two, pressure = 500 kPa, maximum surface velocity = 0.125 m/s, mass = 5.000 kg.

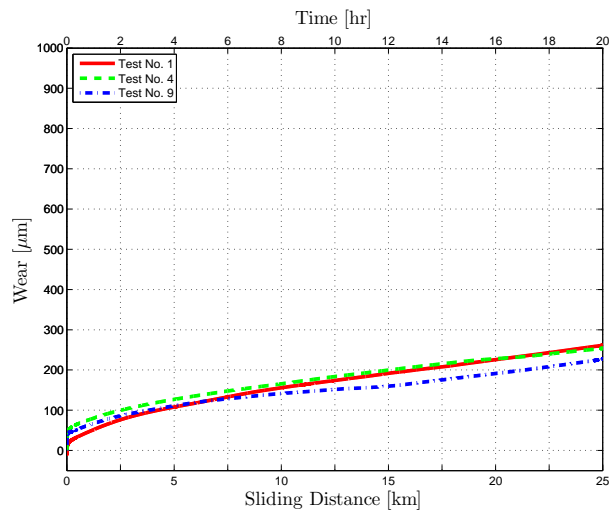


Figure 4.14: Experiment case three, pressure = 202 kPa, maximum surface velocity = 0.55 m/s, mass = 2.045 kg.

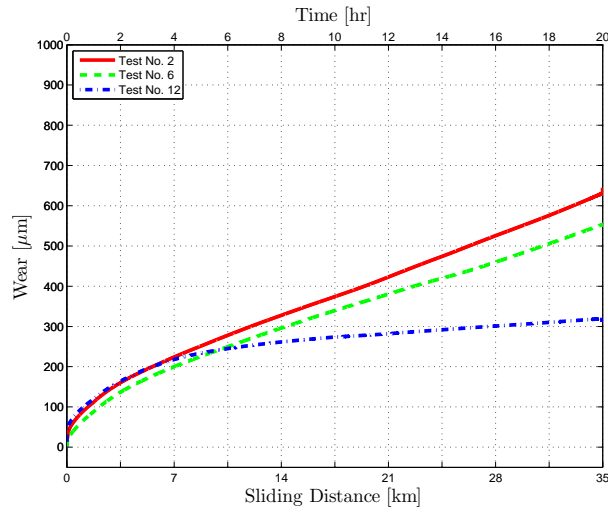


Figure 4.15: Experiment case four, pressure = 445 kPa, maximum surface velocity = 0.69 m/s, mass = 4.442 kg.

used, where the volumetric wear for each hour of reported wave data was calculated using 1) a specific wear rate, e from the model, 2) a normal force, F , derived from Morison's equation, and 3) a sliding distance, s derived from the particular climate's reported wave parameters. For the month of January 2011, a total of 4.5 mm was estimated to have been lost during the theoretical point absorber WEC operation (Fig. 4.17). Additional information was recorded before and after each test run that included the counterface surface roughness measurements (Tbl. 4.4).

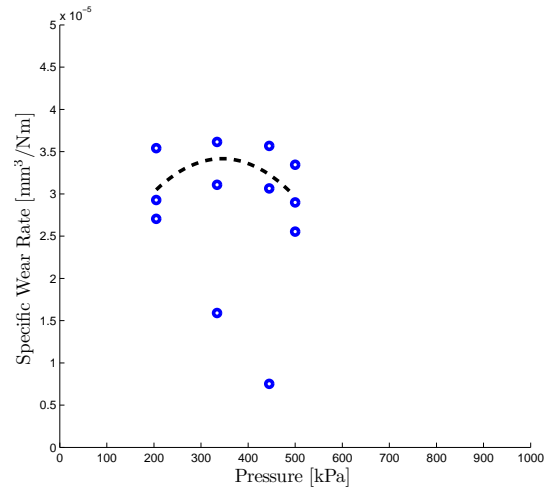


Figure 4.16: Specific wear rates plotted vs. applied bearing pressure for all twelve test runs with the conservative model overlay (dotted line).

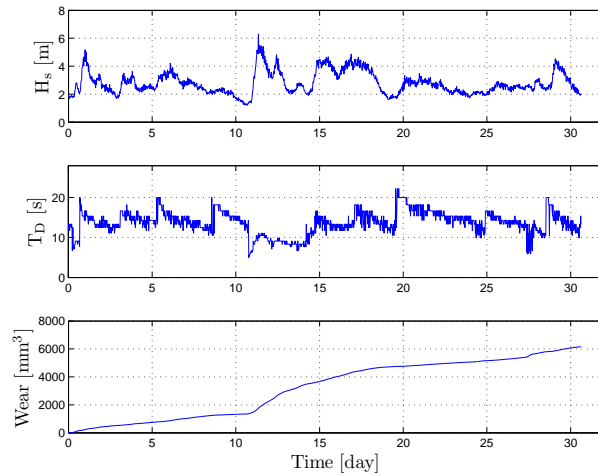


Figure 4.17: An example wear estimation for the month of January 2011.

Table 4.4: Stable wear rates for each test run and their corresponding before and after surface roughness measurements (average, maximum, minimum).

Exp. Case	Test No.	Rate ($\frac{\mu\text{m}}{\text{hr}}$)	Before ($\mu\text{m Ra}$)	After ($\mu\text{m Ra}$)
1	3	18	.58 .69 .48	.71 .84 .56
	8	8	.61 .71 .48	.61 .79 .46
	10	16	.56 .69 .43	.53 .71 .38
2	5	45	.66 .81 .51	.63 .79 .41
	7	37	.61 .76 .53	.51 .64 .43
	11	42	.51 .58 .41	.48 .61 .33
3	1	9	.69 .76 .51	.58 .74 .43
	4	7	.69 .74 .58	.69 .79 .58
	9	8	.53 .69 .46	.53 .66 .41
4	2	25	.74 .79 .69	.64 .74 .58
	6	21	.66 .76 .58	.71 .94 .51
	12	5	.61 .71 .53	.56 .69 .43

4.8 Discussion

This section discusses several factors contributing to the uncertainty in the results. Topics affecting the accuracy of the prediction include the effect of counterface surface roughness, wave modeling, wear data quality, and test stand effects.

4.8.1 Effect of Counterface Roughness

To begin, the effect of surface roughness on the stable wear rate is plainly apparent and as one would expect, a higher roughness generally yields a higher wear rate. Observing experiment case four in particular, test no. 12 yielded a stable wear rate 4 - 5 times smaller with a pre-test surface roughness less than $0.06 \mu\text{m}$ smoother than test no. 2 or 6. Perhaps this result is specific to the experiment (relatively high pressure and frequency oscillation) as the difference between pre-test roughness measurements for experiment cases two and three are similar, yet their subsequent stable wear rates are analogous. It should be noted that there are limits as to how smooth the initial counterface can be as one study showed a roughness of $0.03 \mu\text{m}$ increased the wear rate by 33 times [105]. Experiment case one and four both contain a test run dissimilar to the others while their pre-test roughness measurement differences are negligible, indicating that there may be some other factor affecting the results and warranting more experiments.

From previous experience, the bearing material studied exhibited an unusually higher wear rate for their respective loading conditions in the majority of test runs. Acknowledging the customization of the experimental setup and design, the obvious absence of a transfer film may indicate the need for a better application of pressure and velocity to the bearing sample itself via a different test stand design and/or operation.

4.8.2 Wave Modeling

Second, the method of wave modeling used in this investigation assumes a regular wave, which is not an accurate representation of real seas. Utilizing linear waves and the assumption of the buoy being a perfect wave follower are likely the most influential assumptions within this study. The most rigorous of ocean wave modeling efforts solve the Navier Stokes non-linear differential equation for velocities and pressure fields, yet is only suggested for higher fidelity investigations. However, the success of applying the often used principle of superposition (as many frequency domain wave models do) to the wear rates remains to be seen given the limitations of linear wave theory [92]. Another, more promising approach would be to utilize the WEC dynamic models as inputs to the bearing wear experiments [106].

Choosing NDBC 46229 as the source of ocean surface measurements was designed to allow researchers the freedom of using either time or frequency domain information. Also, for a more complete input to the wave climate, the authors suggest using a more robust method that explicitly presents representative wave spectra [107].

4.8.3 Wear Data Quality and Health Estimations

Third, the health estimation, however unrefined, was possible because of quality wear data. The empirical models yielded few extraordinary anomalies and provided a good basis for regression and validation of the sample size suggestion. Applying the wear algorithm, approximately 6000 mm^3 , or 4.5 mm of bearing material was estimated to be lost during the month long WEC operation. This initial estimate is quite large and could be attributed to several factors, including the material itself,

the loading conditions chosen, the load application via the test stand's design and operation, or the counterface's surface roughness.

Also, a method for how to rectify the fact that wear rates do not exist for each bin within the wave climate has yet to be developed and would constitute a very interesting future work. Although the experiments do not change parameters during the 20 hour tests, future work would require the programming of varying parameters, resulting in more accurate loading conditions. Also, some of the next steps in this research would apply more advanced aspects of PHM by incorporating uncertainty assessment [2] and prognostic evaluation [23].

4.8.4 Test Stand Effects

Fourth, the effects of the test stand on the bearing experiments is inherent in the wear data, so only by modifying the test stand and running the same experiments would the effects be measurable. During testing, the motor was observed to jerk near the crest and trough of the sinusoid velocity profile, indicating poor torque control. This phenomenon occurred with greater intensity during experimental cases with higher pressures, possibly inhibiting transfer film formation. A torque sensor and higher torque motor would be ideal, so as to accurately and smoothly follow the desired velocity profile. Some of the first test stand modifications to produce more accurate results would be the integration of a varying pressure function and time domain velocity profile. Currently, the test stand is limited to constant force application and only after running these initial experiments has it become readily obvious that the test stand is not capable of accurately recreating loading conditions that a bearing sample would see in the field - a much smoother control of the counterface motion is required.

4.8.5 Lessons Learned

Often times PHM is an afterthought in complex system design because of many unanswered questions regarding prognostic requirements and their resulting validation sequence [108]. This research focused on one component of the WEC even as developers work to install production-level devices, where bearing health estimation may be the lowest of priorities. Promoting a scalable approach to classifying bearing wear for WECs early in the growth of the industry can be extremely beneficial to all parties.

4.9 Conclusion

Twelve bearing wear experiments were conducted using a detailed approach suited for polymer bearings installed on a point-absorbing WEC. A stable and linear wear rate was established for each experiment, leading to the use of empirical methods for estimating bearing wear. Not only was essential information gained regarding the limits of the experiments, but the actual research methodology as well. Even though much work remains, progress was made towards careful benchmarking of the test stand and successful employment of PHM research tenets, all while pushing the state of technology for WEC-based bearing health estimation forward.

Acknowledgments

The authors wish to thank Thordon Bearings for supplying the bearing samples used in this study.

Nomenclature

PHM	Prognostics and Health Management
WEC	Wave Energy Converter
T_D	dominant wave period
H_s	significant wave height
η	water surface displacement, a function of x and t
k	wave number
ϕ	water particle velocity potential
F_x	horizontal force imposed on buoy by passing wave
e	specific wear rate
i	bin index (wave height and wave period)
V_i	volumetric wear
c_i	total bin index hours

Chapter 5 – General Conclusion

Three manuscript papers have been presented, outlining the attributes of test stand design and operation affecting the success of system reliability estimations within a prognostics and health management research methodology. While the actuator test stand captures failure information for numerous faults and the bearing test stand measures bearing wear, both essentially collect component health data that is aggregated and used in prognostic algorithms to estimate overall system health. Data from the bearing test stand was post-processed to illustrate an initial attempt at predicting bearing health for a given month. Again, the quality of data used by an aircraft's health management system or wave energy converter's maintenance engineer is especially important, and has yet to be validated on a practicing system or by an approved standard.

5.1 Applications and Future Directions

Obtaining real-time system performance data has become easier with recent technological leaps in electronics and data acquisition. However, real-time failure information is more difficult to achieve, as it is often due to the classifying, filtering, processing, and inferring processes required. And so, flyable test stand research becomes applicable: with known failure models derived from the test stand, the prognostic model can learn the past component performance characteristics and ideally yield a confident health assessment. The contributions within this thesis can be applied to either the current test stand or to the design of a new one,

where the insight and results provided can assist interest researchers in their own projects. With adequate resources, multiple test stands could be built to foster actuator prognostic research, expand actuator failure model databases, and improve confidence in actuator health estimations. More research and work is needed to address the faults chosen for the failure experiments, because often times faults progress to failure at the extremes of the time scale - milliseconds or years, and thus does not bode well for modeling algorithms.

Second, as ocean renewable investment grows, it is important that system health and reliability estimations be derived from an accepted research methodology so that comparison between studies is efficient and scalable. The bearing wear data is an ideal candidate for integration into a system reliability assessment due to its simplicity and impact on multiple sub-systems. By using a similar approach to that presented in manuscript three, future wear experiments can effectively contribute to the total bearing health model and succeeding wave device reliability model. Further, verification and validation of this research approach would enable more informed WEC design and maintenance decisions.

In closing, this thesis has highlighted the importance of test stand design and operation within research efforts aimed at assessing component reliability and health. Many factors have been shown to affect the success of failure experiments and it is the author's belief that learning what factor carries the largest uncertainty will be the key to implementing effective prognostic solutions.

Bibliography

- [1] Koopmans, M., and Tumer, I. Y., 2010. “Function-based analysis and re-design of a flyable electromechanical actuator test stand”. In Proceedings of the ASME IDETC/CIE Conference.
- [2] Tang, L., Kacprzynski, G., Goebel, K., and Vachtsevanos, G., 2008. “Methodologies for uncertainty management in prognostics”. In IEEE Aerospace Conference.
- [3] Wertz, J., and Larson, W., 1999. *Space mission analysis and design*. Microcosm.
- [4] Gerwick, B., 2007. *Construction of marine and offshore structures*. CRC Press.
- [5] Vachtsevanos, G., Lewis, F. L., Roemer, M., Hess, A., and Wu, B., 2006. *Intelligent Fault Diagnosis and Prognosis for Engineering Systems*. John Wiley and Sons.
- [6] Uckun, S., Goebel, K., and Lucas, P. J. F., 2008. “Standardizing research methods for prognostics”. In International Conference on Prognostics and Health Management, Denver, CO.
- [7] Goebel, K., Saha, B., Saxena, A., Celaya, J., and Christophersen, J., 2008. “Prognostics in battery health management”. In Proc. IEEE.
- [8] Balaban, E., Saxena, A., Narasimhan, S., Roychoudhury, I., Goebel, K. F., and Koopmans, M. T., 2010. “Airborne electro-mechanical actuator test stand for development of prognostic health management systems”. In Annual Conference of the Prognostics and Health Management Society.
- [9] Jensen, S. C., Jenney, G. D., Raymond, B., and Dawson, D., 2000. “Flight test experience with an electromechanical actuator on the f-18 systems research aircraft”. In Digital Avionics Systems Conference.
- [10] NTSB, 1989. Aircraft accident report: United airlines flight 232 mcdonnell douglas DC-10 sioux gateway airport, sioux city, iowa, july 19,1989. Accident report, National Transportation Safety Board.
- [11] NTSB, 2000. Aircraft accident report: Loss of control and impact with the pacific ocean, alaska airlines flight 261, MD-83, N963AS, about 2.7 miles

- North of anacapa island, California, January 31, 2000. Accident report, National Transportation Safety Board.
- [12] DOD, 2009. Predicting faults and determining life of electro-mechanical actuation system for engine and aerospace applications, AF093-176. On the WWW. www.dodsbir.net/Sitis/archives_scan.asp?sol=093.
 - [13] Jenney, G., 2005. Advanced electromechanical actuation system for jet blast deflectors. Tech. rep., Australian Transport Safety Bureau.
 - [14] Tesar, D., and Krishnamoorthy, G., 2008. “Intelligent electromechanical actuators to modernize ship operations”. *American Society of Naval Engineers*, **120**(3), pp. 77–88.
 - [15] Fuerst, D., Hausberg, A., and Neuheuser, T., 2008. “Experimental verification of an electro-mechanical actuator for a swashplateless primary and individual helicopter blade control system”. In Proc. American Helicopter Society 64th Annual Forum.
 - [16] Janker, P., Claeysen, F., Grohmann, B., Christmann, M., T. Lorkowski, R. L., Sosniki, O., and Pages, A., 2008. “New actuators for aircraft and space applications”. In Proc. International Conference on New Actuators.
 - [17] Schwabacher, M., Samuels, J., and Brownston, L., 2002. The NASA integrated vehicle health management technology experiment for x-37. Tech. rep., NASA.
 - [18] Hvass, P. B., and Tesar, D., 2004. “Condition Based Maintenance for Intelligent Electromechanical Actuators”. MS Thesis, The University of Texas at Austin, Austin, TX.
 - [19] Schwabacher, M., 2005. “A survey of data-driven prognostics”. In Proc. American Institute of Aeronautics and Astronautics Conference.
 - [20] Schwabacher, M., and Goebel, K., 2007. “A survey of artificial intelligence for prognostics”. In Proc. AAAI Fall Symposium, N. A. R. Center.
 - [21] Hess, A., Calvello, G., and Firth, P., 2005. “Challenges, issues, and lessons learned chasing the ‘big p’: Real predictive prognosis part 1”. In IEEE Aerospace Conference.
 - [22] Hess, A., Calvello, G., Firth, P., Engel, S. J., and Hoitsma, D., 2006. “Challenges, issues, and lessons learned chasing the ‘big p’: Real predictive prognosis part 2”. In IEEE Aerospace Conference.

- [23] Saxena, A., Celaya, J., Balaban, E., Goebel, K., Saha, B., Saha, S., and Schwabacher, M., 2008. “Metrics for evaluating performance prognostic techniques”. In International Conference on Prognostics and Health Management, Denver, CO.
- [24] Byington, C., Watson, M., and Edwards, D., 2004. “Data-driven neural network methodology to remaining life predictions for aircraft actuator components”. In Proc. IEEE Aerospace Conference.
- [25] Ma, L., 2007. “Condition monitoring in engineering asset management”. In Proc. 12th Asia-Pacific Vibration Conference.
- [26] Balaban, E., Saxena, A., Goebel, K., Byington, C., Watson, M., Bharadwaj, S., and Smith, M., 2009. “Experimental data collection and modeling for nominal and fault conditions on electro-mechanical actuators”. In Annual Conference of the Prognostics and Health Management Society.
- [27] Balaban, E., Saxena, A., Bansal, P., Goebel, K., Stoelting, P., and Curran, S., 2009. “A diagnostic approach for electro-mechanical actuators in aerospace systems”. In IEEE Aerospace Conference.
- [28] Bodden, D. S., Clements, N. S., Schley, B., and Jenney, G. D., 2007. “Seeded failure testing and analysis of an electro-mechanical actuator”. In IEEE.
- [29] Brown, E., McCollom, N., Moore, E., and Hess, A., 2007. “Prognostics and health management: A data-driven approach to supporting the f-35 lightning ii”. In IEEE Aerospace Conference.
- [30] Mahadevan, S., and Smith, N., 2003. System risk assessment and allocation in conceptual design. Technical report, NASA.
- [31] Billinton, R., and Allan, R. N., 1992. *Reliability Evaluation of Engineering Systems: Concepts and Techniques*. Plenum Press, New York.
- [32] Nikolaidis, E., Ghiocel, D., and Singhal, S., 2005. *Engineering Design Reliability Handbook*. CRC Press.
- [33] Dodson, B., and Nolan, D., 2002. *Reliability Engineering Handbook*. QA Publishing, Tucson, AZ.
- [34] O’Connor, P., Newton, D., and Bromley, R., 2002. *Practical Reliability Engineering*. John Wiley & Sons.
- [35] Koopmans, M., Mattheis, C., and Lawrence, A., 2009. Electro mechanical actuator test stand for in-flight experiments. Senior project report, California Polytechnic State University, San Luis Obispo, CA.

- [36] Denson, W., Chandler, G., Crowell, W., Clark, A., and Jaworski, P., 1994. *Nonelectric Parts Reliability Data*. IIT Research Institute, New York, N.Y.
- [37] DOD, 1991. *Military Handbook - Reliability Prediction of Electronic Equipment (MIL-HDBK-217F)*. DOD, Washington, D.C.
- [38] Reliability engineering basics, 2010. <http://reliabilityeducation.com>.
- [39] DOD, 1984. MIL-STD-1629A: Procedures for performing a failure mode effects and criticality analysis. Tech. rep., DOD.
- [40] AIAG, 2008. Potential failure mode and effects analysis. Tech. rep., Automotive Industry Action Group.
- [41] Vesely, W., Goldberg, F., Roberts, N., and Haasl, D., 1981. *Fault Tree Handbook (NUREG-0492)*.
- [42] Modarres, M., Kaminskiy, M., and Krivtsov, V., 1999. *Reliability Engineering and Risk Analysis: A Practical Guide*. Marcel Dekker, New York.
- [43] Kiureghian, A., Ditlevsen, O., and Song, J., 2007. “Availability, reliability and downtime of systems with repairable components”. *Journal of Reliability Engineering & System Safety*, **92**(2), pp. 231–242.
- [44] THK HSR R basics, 2010. https://tech.thk.com/en/products/thk_cat_main_fourth.php?id=1141.
- [45] GM, 2011. Vehicle diagnostics. On the WWW. www.onstar.com/web/portal/vehiclediagnosics.
- [46] Boeing, 2011. Airplane health management. On the WWW. www.boeing.com/commercial/ams/mss/brochures/airplane_health.html.
- [47] ATSB, 2010. In-flight uncontained engine failure overhead batam island, indonesia, 4 november 2010, VH-OQA, Airbus A380-842. Preliminary report AO-2010-089, Australian Transport Safety Bureau.
- [48] Shetty, P., Mylaraswamy, D., and Ekambaram, T., 2008. “A hybrid prognostic model formulation and health estimation of auxiliary power units”. *Journal of Engineering for Gas Turbines and Power*, **130**(2), March.
- [49] Saha, B., Goebel, K., Poll, S., and Christophersen, J., 2009. “Prognostics methods for batter health monitoring using a bayesian framework”. *IEEE Transactions on Instrumentation and Measurement*, **58**(2), pp. 291–296.
- [50] Sankararaman, S., Ling, Y., Shantz, C., and Mahadevan, S., 2009. “Uncertainty quantification in fatigue damage prognosis”. In Annual Conference of the Prognostics and Health Management Society.

- [51] Saxena, A., Celaya, J., Saha, B., Saha, S., and Goebel, K., 2010. “Evaluating prognostics performance for algorithms incorporating uncertainty estimates”. In IEEE Aerospace Conference.
- [52] Deshmukh, P., and Bernhardt, K. L. S., 2000. “Quantifying uncertainty in bridge condition assessment data”. In Mid-Continent Transportation Symposium Proceedings.
- [53] The Prognostics Center of Excellence at NASA Ames Research Center. <http://ti.arc.nasa.gov/tech/dash/pcoe/>.
- [54] Thunnissen, D. P., 2005. “Propagating and mitigating uncertainty in the design of complex multidisciplinary systems”. PhD Thesis, California Institute of Technology, Pasadena, CA.
- [55] Hoyle, C., Tumer, I., Mehr, A., and Chen, W., 2009. “Health management allocation for conceptual system design”. *ASME Journal of Computing & Information Sciences in Engineering*, **9**(2).
- [56] Millar, R., 2008. “Defining requirements for advanced phm technologies for optimal reliability centered maintenance”. In IEEE Aerospace Conference.
- [57] CBM and Enterprise Health Management Panel Session. 2010 Annual Conference of the PHM Society.
- [58] Melchers, R., ed., 1999. *Structural Reliability Analysis and Prediction, 2nd edition*. John Wiley & Sons, Chichester, United Kingdom, pp. 34–45.
- [59] Draper, D., 1995. “Assessment and propagation of model uncertainty”. *Journal of the Royal Statistical Society, Series B (Methodological)*, **57**(1), pp. 45–97.
- [60] Khalak, A., and Goebel, K., 2008. “Real-time probabilistic forecasting of wear degradation using a macro-scale physical model”. In IEEEAC. Paper number 1527.
- [61] Huff, E., Tumer, I., Barszcz, E., Dzwonczyk, M., and McNames, J., 2002. “Analysis of maneuvering effects on transmission vibrations in an ah-1 cobra helicopter”. *Journal of the American Helicopter Society*, **47**(1), pp. 42–49.
- [62] Saha, B., and Goebel, K., 2008. “Uncertainty Management for Diagnostics and Prognostics of Batteries using Bayesian Techniques”. In IEEE.
- [63] Tang, L., DeCastro, J., Kacprzynski, G., Goebel, K., and Vachtsevanos, G., 2010. “Filtering and prediction techniques for model-based prognosis and uncertainty management”. In IEEE Prognostics & System Health Management Conference.

- [64] Barkman, A., 1998. "Critical loads - assessment of uncertainty". Doctoral Thesis, Lund University, Lund, Sweden.
- [65] Koopmans, M., Hooven, R., and Tumer, I., 2010. "Reliability based design recommendations for an electromechanical actuator test stand". In Annual Conference of the Prognostics and Health Management Society.
- [66] UltraMotion, 2011. The bug. <http://ultramotion.com/products/bug.php>.
- [67] Moog, 2010. Multi-purpose actuators & servoactuators. <http://www.moog.com/products/actuators-servoactuators/multi-purpose/linear-actuators/model-801-973/>.
- [68] Roarks, 2000. *Roarks Formula for Stress and Strain Ed. 5 , Table 8.8/1a & Table 8.1/1e*. John Wiley, Washington, DC.
- [69] Budynas, R., and Nisbett, K., 2001. *Shigleys Mechanical Engineering Design*. McGraw-Hill, New York, New York.
- [70] Papalambros, P., and Wilde, D., 2000. *Principles of Optimal Design: Modeling and Computation 2d Ed*. Cambridge University Press, New York, New York.
- [71] Hinrichsen, D., 1999. *Coastal Waters of the World: Trends, Threats, and Strategies*. Island Press.
- [72] Cruz, J., 2008. *Ocean wave energy: current status and future perspectives*. Springer.
- [73] Ocean power technologies, 2011. <http://www.oceanpowertechnologies.com/>.
- [74] Wave dragon, 2011. <http://www.wavedragon.net/>.
- [75] Wavegen, 2011. http://www.wavegen.co.uk/what_we_offer_limpet.htm.
- [76] Yemm, R., 2003. Pelamis wec, full scale joint system test. Summary report, Ocean Power Delivery Ltd. http://www2.env.uea.ac.uk/gmmc/energy/energy_pdfs/pelamis_joint_system_test.pdf.
- [77] Floating power plant, 2011. <http://floatingpowerplant.com/>.
- [78] Aquamarine power, 2011. <http://www.aquamarinepower.com/>.
- [79] Cowper, D., Kolomojcev, A., Danahy, K., and Happe, J., 2006. "Uscg polar class aft sterntube bearing design modifications". In International Conference on Performance of Ships and Structures in Ice.

- [80] McCarthy, D. M. C., and Glavatskih, S. B., 2009. “Assessment of polymer composites for hydrodynamic journal-bearing applications”. *Lubrication Science*, **21**(8), pp. 331–341.
- [81] Ren, G., and Muschta, I., 2010. “Challenging edge loading: A case for homogeneous polymer bearings for guidevanes”. *International Journal on Hydropower and Dams*, **17**(6), pp. 121–125.
- [82] Wang, J., Yan, F., and Xue, Q., 2009. “Tribological behavior of ptfе sliding against steel in sea water”. *Wear*, **267**, pp. 1634–1641.
- [83] Ginzburg, B., Tochil’nikov, D., Bakhareva, A., and Kireenko, O., 2006. “Polymeric materials for water-lubricated plain bearings”. *Russian Journal of Applied Chemistry*, **79**, pp. 695–706.
- [84] Rymuza, Z., 1990. “Predicting wear in miniature steel-polymer journal bearings”. *Wear*, **137**(2), pp. 211–249.
- [85] W.D. Craig, J., 1964. “Operation of ptfе bearings in sea water”. *Lubrication Engineering*, **20**, pp. 456–462.
- [86] Tsuyoshi, K., Kunihiro, I., Noriyuki, H., Shozo, M., and Keisuke, M., 2005. “Wear characteristics of oscillatory sliding bearing materials in seawater”. *Journal of the Japan Institution of Marine Engineering*, **40**(3), pp. 402–407.
- [87] Caraher, S., Chick, J., and Mueller, M., 2008. “Investigation into contact and hydrostatic bearings for use in direct drive linear generators in submerged wave energy converters”. In International Conference on Ocean Energy.
- [88] Gawarkiewicz, R., and Wasilczuk, M., 2007. “Wear measurements of self-lubricating bearing materials in small oscillatory movement”. *Wear*, **263**, pp. 458–462.
- [89] ASTM, 2009. “G176 - 03(2009) standard test method for ranking resistance of plastics to sliding wear using block-on-ring wear test, cumulative wear method”. <http://www.astm.org/Standards/G176.htm>.
- [90] Tucker, M., and Pitt, E., 2001. *Waves in ocean engineering*. Oxford, Elsevier.
- [91] Holthuijsen, L., 2007. *Waves in oceanic and coastal waters*. New York, Cambridge University Press.
- [92] Young, I., 1999. *Wind generated ocean waves*. Netherlands, Elsevier.
- [93] FERC, 2011. Hydrokinetic projects. On the WWW. <http://www.ferc.gov/industries/hydropower/indus-act/hydrokinetics.asp>.

- [94] CDIP, 2011. Coastal data information program. On the WWW. <http://cdip.ucsd.edu/>.
- [95] NDBC, 2011. National data buoy center. On the WWW. <http://www.ndbc.noaa.gov/>.
- [96] Tucker, M., 1991. *Waves in Ocean Engineering: Measurement, Analysis, and Interpretation*. Ellis Horwood, LTD.
- [97] Steele, K., and Mettlach, T., 1993. "NDBC wave data - current and planned". In *Ocean Wave Measurement and Analysis - Proceedings of the Second International Symposium*, pp. ASCE, 198–207.
- [98] Ochi, M., 1998. *Ocean waves*. Cambridge, Cambridge University Press.
- [99] Dean, R., and Dalrymple, R., 1991. *Water Wave Mechanics for Engineers and Scientists*. World Scientific.
- [100] Morison, J., O'Brien, M., Johnson, J., and Schaaf, S., 1950. "The force exerted by surface waves on piles". *Petroleum Transactions, AIME*, **189**, pp. 149–154.
- [101] Agerschou, H., and Edens, J., 1965. "Fifth and first order wave - force coefficients for cylindrical piles". In *ASCE Coastal Engr. Speciality Conf. Ch. 10*. pp. 239.
- [102] Montgomery, D., 2009. *Design and Analysis of Experiments 7th ed.* John Wiley & Sons.
- [103] Thordon, 2011. Sxl. On the WWW. <http://www.thordonbearings.com/clean-power-generation/tidalcurrentpower/design>.
- [104] Marcus, K., Ball, A., and Allen, C., 1991. "The effect of grinding direction on the nature of the transfer film formed during the sliding wear of ultra-high molecular weight polyethylene against stainless steel". *Wear*, **151**(2), pp. 323–336.
- [105] Marcus, K., and Allen, C., 1994. "The sliding wear of ultrahigh molecular weight polyethylene in an aqueous environment". *Wear*, **178**(2), pp. 17–28.
- [106] Ruehl, K., Brekken, T., Bosma, B., and Paasch, R., 2010. "Large-scale ocean wave energy plant modeling". In *IEEE CITERES*.
- [107] Lenee-Bluhm, P., 2010. "The wave energy resource of the US Pacific northwest". MS Thesis, Oregon State University, Corvallis, OR.
- [108] Ferrell, B. Joint strike fighter program fielded systems presentation. 2010 Annual Conference of the PHM Society.

